

CONTENTS — A through G

Spreading of Mars' Southern Polar Cap and Climatic-Structural Signals <i>P. Aftabi</i>	8059
The Impact of Atmospheric Methane on Martian Polar Climate and Subsurface Ice <i>P. D. Archer Jr., A. A. Pavlov, and P. H. Smith</i>	8063
Near-Perihelion Global Dust Storm and the Stability of the Perennial South Polar Cap on Mars <i>B. P. Bonev, P. B. James, G. B. Hansen, D. A. Glenar, and J. E. Bjorkman</i>	8064
Using Silicon and Hydrogen Gamma Rays for the Simultaneous Determination of Dry-Layer Thickness and Sub-Surface Ice Content in the Polar Regions of Mars <i>W. V. Boynton, D. M. Janes, M. Finch, and R. M. S. Williams</i>	8026
Landscape Evolution and the Reincarnation of the Southern Residual Ice Cap <i>S. Byrne and M. T. Zuber</i>	8035
A Field Demonstration of Thermal Drilling Technology for the Chronos Scout 2011 Mission <i>G. Cardell, M. Smith, M. Hecht, R. Kowalczyk, C. Mogensen, and A. Behar</i>	8088
Monitoring and Physical Characterization of the South Seasonal Cap of Mars from Omega Observations <i>S. Douté, Y. Langevin, F. Schmidt, B. Schmitt, M. Vincendon, J. P. Bibring, F. Poulet, E. Deforas, and B. Gondet</i>	8030
Simulation of Dust Sedimentation on the Calibration Targets for the Surface Stereo Imager Onboard the Phoenix Mars Lander 2007 <i>L. Drube, M. B. Madsen, M. Olsen, J. Jørgensen, D. Britt, M. Lemmon, C. Shinohara, and P. Smith</i>	8012
A Better Flow Law for Dirty, Very Slow Ice <i>W. B. Durham, A. Pathare, L. A. Stern, and S. H. Kirby</i>	8104
Effect of a Surface Cover of Dust on Sublimation Rates in the Polar Layered Deposits on Mars <i>M. D. Ellehøj and C. S. Hvidberg</i>	8021
Quantitative Comparison Between Burial Depths of Hydrogen Inferred from Neutron Data and Ground-Ice Stability Models <i>W. C. Feldman, M. T. Mellon, O. Gasnault, B. Diez, R. C. Elphic, J. J. Hagerty, D. J. Lawrence, S. Maurice, and T. H. Prettyman</i>	8051
Stratigraphy and Accumulation Rates of the North Polar Layered Deposits with Implications for Flow <i>K. E. Fishbaugh and C. S. Hvidberg</i>	8038
Formation of the Martian North Polar Gypsum Deposit During the Amazonian <i>K. E. Fishbaugh, F. Poulet, Y. Langevin, V. Chevrier, and J-P. Bibring</i>	8041
Sensitivity of D/H in Mars Atmosphere to Time Varying Processes in the Water Cycle, Water Reservoir Sizes and Exchange Rates; What D/H History Might be Found by Drilling in the North Polar Cap and What It Might Mean <i>D. A. Fisher</i>	8004

Ice Caps, Glaciers and Gullies: The Effect of Obliquity on Martian Climate <i>F. Forget, F. Montmessin, B. Levrard, R. M. Haberle, J. W. Head, and J.-B. Madeleine</i>	8106
Unconformity and Bedding Orientations in Planum Boreum, Mars: Preliminary Results and Discussion <i>C. M. Fortezzo and K. L. Tanaka</i>	8079
Scenarios for the Formation of Chasma Borealis, Mars <i>R. Greve</i>	8002
Photometric Signatures of Liquid Water in JSC Mars-1 Regolith Simulant <i>K. Gunderson, B. Lüthi, P. Russell, and N. Thomas</i>	8060

Spreading of Mars' Southern Polar Cap(MPC) and Climatic-Structural Signals

Pedram Aftabi

Tectonics Group, Geological Survey of Iran, PO Box 131851-1494, Tehran, Iran,

Ped_Aftabi@yahoo.com, p-aftabi@gsi-info.com

The White rock on Mars is an enigmatic geological formation within a large Southern Hemisphere. Despite the high reflectivity of the Mars image, the MPC is currently believed to consist of ice [1]. Numerical Investigation of Ice-Lobe-Permafrost Interaction show that the ice acts as viscous material [2] like salt [3, 7]. The amount of ice increased toward the South Pole [4, 5, and 6]. Detailed analysis of the data indicates that the ice-rich layer resides beneath a hydrogen-poor upper layer. The thickness of the upper layer decreases from about 75 cm at -42° to about 20 cm at -77° . The amount of ice in the lower layer is between 20 and 50 wt% (weight percent), with a best estimate of 35 wt% [4, 5, 6]. We do not know exactly about the 65 % rest of the wt% of the lower layer. The upper layer consists of polygonal pattern of fractures[8] similar to the salt and mud flats on Earth[7]. With using model of the regional topography [8], provided interpretations of the external shape of the cap and internal structure which are responsible for a viscous fluid model (subscribed). A salt-cemented crusty material called "duricrust" and also uncemented material are found at NASA's exploration sites [8]. There appears to be a global crust of salt enriched materials on the surface, probably in the form of (Mg, Na) SO₄, NaCl, and (Mg, Ca) CO₃, [10] and jarosite [11]. On Mars, any liquid water would have to be a highly concentrated brine solution [12], and eventually, the brine pockets would have dried to form evaporate [13]. However, the sulfate salts epsomite, glauberite, and thenardite have similar properties (hardness, cleavage density, solubility, and viscosity) to halite and gypsum and thus likely deform into similar structures both on Earth and Mars. Polygonal patterns similar to those on salt flats on Earth, are common in middle and high latitudes of Mars [8] and suggest stresses induced by temperature cycles, or probably formed by stresses induced by seasonal and daily freezing and warming cycles of ice in the ground. One of the important uses of salt includes de-icing of roads, since it lowers the freezing point of water. It is important to mention that, the simple events on Earth are keys for Martian conditions. The average temperature on Mars is about -55°C , Martian surface temperatures range widely from as little as -133°C , at the winter pole to almost 27°C , on the day side during summer[8]. Unpublished laboratory experiments by the author found a 22×20 mm pool of a chloride and sulfate brine to freeze to a highly viscous mixture of brine droplets with crystals of salt and ice at temperatures between -11 to -22°C . Other experiments (by author) at -11 to -30°C showed that 10 ml/l brine generated 1ml/l of mixed salt and ice after 180 minutes and 1.6 ml/l after 540 minutes. The mix compacted to 1.4 & 1.2 ml/l after 1440 and 1890 minutes respectively in Earth's gravity which is 3 more times than on Mars. Although the highly solution salt brine never frizzed in the temperature change even to -30°C . This work suggests that primary beds of salt may crystallize very rapidly on surface of Mars, and a very high viscous icy-brine mixture may exist very deeply below the salt cover. NASA's Opportunity rover has demonstrated some rocks on Mars probably formed as deposits at the bottom of a body of gently flowing salt water[8]. The most of such brines would tend to sink deep into the megaregolith, they could be preserved locally at relatively high elevations as aquifers (or frozen pale aquifers) perched between ground ice and crystalline salts, another words the ice considered on top of the brine and salt deposits [14]. However In author's freezing experiments(here) the top layer frizzed as a very thin ice and salt mixture(with less than 20% salt), the middle layer(with more than 90% of total thickness) was thick high viscous liquid icy-brine with high amount of salt solution and the lower part was salt and ice compacted crystals deposits. Monitoring the deformation of passive marker grids confirmed the finding and inferences of previous workers modeling gravity spreading [e.g. 9, 16]. Extrusions of polydimethylsiloxane (PDMS 36), a transparent viscous polymer [15] model not only the shapes of viscous extrusions and their internal structures[7], but also the strain of a flowing sheet like the southern pole of Mars(Fig1). PDMS micro droplets on a silicon wafer exhibit strikingly different shapes under spreading [17], but in two external shapes on meso scales (subscribed). Further experiments reveal that PDMS develops dynamical layering, on a high - energy surface [17]. In large scales the dynamical layering are pseudostratigraphic layers and are related to folding. The viscous sheets spreading by gravity (like ice glaciers) advance by the top surface rolling over the advancing front to attach to an expanding basal contact(Fig1). This induces a single kinematic caterpillare-like tank-track fold with a hinge parallel to the flow front in internal passive marker layers (Fig 1k). The analogue modeling and photo geology suggest that the Southern polar cap act as a viscous flowing material(subscribed) in the lower part and, brittle ductile in the uppermost part(subscribed). A sheet of viscous material(ice?) Flows slowly in cold atmosphere temperature (Figs. 2g, h, I, j & 3). The exaggeration of the three experiments in different temperatures compared with positions of the spreading viscous fluids (salt) on Earth, Mars and Venus(Figs 2g,h,I,j&3). The experiments with simple rectangular sheets of flowing material (PDMS) showed that the flow rate have a positive relationship with temperature. The field studies and measurements on salt glacier suggest that the salt elastic movements are mainly related to the humidity [3]. In PDMS sheets (Figs 2 g-j) with increasing temperature rate of flow increased, but the sheet contracted and moved backward, because of the decreasing in temperature in 3 seconds. Later PDMS continued to be spread progressively (Fig3) further in flow direction, outward (Fig3). The measurements suggest that the rate of flow in the surface Southern cap of the Mars(MPC) planet is much slower than Earth (Figs 2j-g & 3). In essence, 3D flows can be considered as complex combinations of irrigational and rotational strains that vary in space with time. Finite strains are only strongly rotational near the bottom boundary, at and below the axial surface of the kinematics fold growing behind the advancing flow front (Fig1). Experiments showed that with increasing temperature to 78°C PDMS spread 2 times faster than room temperature (Fig2g-j), means that a dynamically changing atmosphere can generated minor folds in spreading sheets. Viscous sheets flow in similar manner (Figs 1, 2&3), but with different height and size. The change of the rate of spreading, erosion, and (ice-salt) supply (above or below) generated folds in the spreading sheets (Figs 1, 2). The experiments suggest that the seasonal changes are important to the change in the rate of spreading.

References:

- [1] Vaniman, D.T., & Others, 2004, Nature, Vol. 431, pp. 663-665. [2] Cutler, P.M. & Others., 2000, Journal of Glaciology 46(153), pp.311-325. [3] Aftabi, P. & Others, 2005, Radar Investigations of Planetary and terrestrial environments, abstract, Houston, Texas. [4] Boynton, W. V. and Others, 2002, Science 297:81-85. [5] Feldman, W.C. and Others, 2002, Science, Vol.297, no.5578, pp.75-78. [6] Mitrofanov, I. and Others, 2002, Science 297, pp.78-81. [7] Talbot, C.J., & Aftabi, P., 2004, Journal of the geological Society, London, Vol.161, pp.321-334. [8] <http://www.nasa.gov/>. [9] Brun, J.P., & Merle, O., 1985, Tectonics, 4, pp.705-719. [10] Lane, M.D., & Christensen, P.R., 1998, ICARUS 135, pp.528-536. [11] Papike, J.J., & Others, In Press, Advances in Space Research 33, pp.1244-1246. [12] Landis, G.A., 2001, Astrobiology, Vol.1, No.2, pp.161-164. [13] Mancinelli, R.L. and Others, 2004, Advances in Space Research 33, pp.1244-1246. [14] Knauth, L.P. and Burt, D.M., 2002, Icarus 158, pp.267-271. [15] Weijermars, R., 1986, Naturwissenschaften, Vol.73, S, p.33 [16] Ramberg, H., 1981, Gravity, Deformation and the Earth's crust, Academic Press, London. [17] Heslot, F. & Others, 1989, Nature 338, pp.640.

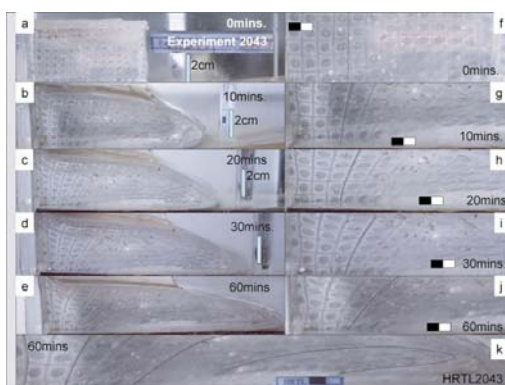


Fig1-Inferred evolution of a rectangular spreading sheet. **a)**The primary state at 0 minutes. **b)**After 10 minutes spreading. **c)** After 20 minutes of spreading. **d)**After 30 minutes spreading. **e)**After 60 minutes spreading. **f)** Strain markers after 0 minutes. **g)** Strain markers after 10 minutes. **h)** Strain markers after 20 minutes. **i)** Strain markers after 30 minutes. **j)** Strain markers after 60 minutes. **k)** Strain markers and deformation lines with caterpillar tank track folding in the termination.

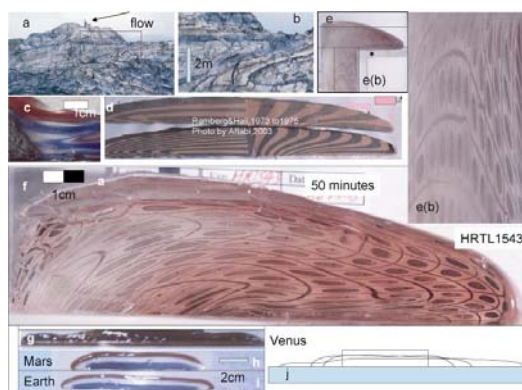


Fig. 2-a&b) The northern glacier at Kuh-e-Namak Dashti (Zagros), with recumbent and rotational recumbent refolds, in different scales. **c)** Unpublished experiment by author showing the internal structure of a PDMS glacier over bedrock of about 30 degrees slope, with two times change in the flow rate. The experiments show similar refolded folds with natural glaciers. The vergence of folds in the profile shows the flow direction to the right. **d)** Originally rectangular blocks of silicone putty which have spread under their own weight in the centrifugal field in a centrifuge. The base of these was coherent to a rigid substratum. The deformation pattern is shown by sheets of silicone with unlike colors. The experiment was performed by Hall [16]. The patterns show similarities with Fig1. **e,e(b)&f)** Different photos of an experiment H1543 by Author show models of viscous extrusions. Traces of deformation lines and strain ellipsoids of the spreading of a single diapir flow upward and sideways by push from behind in the stem. **g)** Gravity spreading of PDMS sheet in primary scale (as shown in Figj) when the temperature increased to 78 degrees c. **h)** Spreading of a primary sheet (as shown on Fig j) when the temperature decreased to lower than -12 degrees c. **i)** Spreading of a primary sheet (as shown on Fig j) under normal room temperature of about 20 degrees c. **j)** Comparison of the spreading of the originally rectangular same size PDMS sheets in different temperatures. The exaggeration of these experiments suggest changes in the rate of spreading of the same size sheets in planets with different humidity. There is lack of considering temperature in the previous workers on modeling.

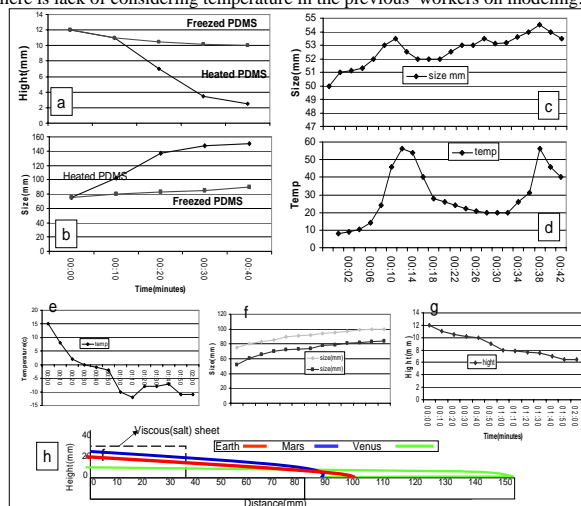


Fig3-PDMS spreading sheet of the originally same size rectangular sheets with considering temperature as a factor in spreading. **a&b)**A comparison of height and size of similar sheets under different atmospheric temperature. **c&d)**Show a positive relationship between changes in the atmospheric temperature and rate of spreading. **e,f&g)**An experiment of an originally rectangular sheet of PDMS in fridge show that with decreasing temperature, the rate of flow decreased but it was continuous. The height of the spreading sheet decreased slowly in this experiment, in compare to the normal room temperature. **h)**A comparison between change in the rate of spreading in primary same size sheets under different temperatures. The exaggeration of these experiments is a key to understanding changes in the flow rates of same size viscous fluids in three planets of the solar system. The experiments suggest that the seasonal changes are important to the change in the rate of spreading. This change in the flow rate may generated 8 major circumferential structural signals(folds-fractures) on MPC.

THE IMPACT OF ATMOSPHERIC METHANE ON MARTIAN POLAR CLIMATE AND SUBSURFACE ICE. P. D. Archer, Jr., A. A. Pavlov, and P. H. Smith, Lunar and Planetary Laboratory, University of Arizona, Tucson, AZ, 85721, darcher@lpl.arizona.edu.

Introduction: The detection of trace amounts of methane in the Martian atmosphere by three separate groups in 2004 [1-3] has generated a debate focused mainly around the possible sources and sinks on Mars. However, methane is a powerful greenhouse gas and, with an atmospheric lifetime on the order of hundreds of years, could play a role in Martian climate. Atmospheric methane could increase the Martian surface temperature, which affects both the amount of water vapor in the atmosphere (another important greenhouse gas) as well as the potential for liquid water at the surface.

Transient Liquid Water Potential. Richardson and Mischna [4] introduce the term transient liquid water potential (TLWP) to describe locations on Mars that have surface temperatures and pressures that fall between the melting point and boiling point of water. They point out that although the atmospheric water vapor pressure is so low that liquid water cannot exist in equilibrium, the lower latent heat of melting compared with evaporation allows for the possibility of transient liquid water. Richardson and Mischna use a GCM to map regions on Mars that have a high enough maximum daily surface temperature and pressure for water to exist.

Just Add Water. Another obvious requirement to have liquid water at or near the surface of Mars is that there must be water ice present. Under current Martian conditions, areas with TWLP fall primarily between 30N and 30S, an area where no surface or near-surface ice deposits are expected. However, different orbital parameters change this picture. If the L_s of perihelion is changed from its current value of 251 to 71 (making northern summer coincide with perihelion), areas with TWLP migrate northward, with some areas as high as 70N experiencing a few days per year where liquid water is possible.

Furthermore, recent numerical results indicate that Martian obliquity is highly variable with an average value over the past 10 Myr of 31.468° and a maximum value of 46.859° over the same time period [5]. Increasing obliquity to 45° causes areas with TWLP to migrate even further north than the effect of precession of perihelion.

Richardson and Mischna make the observation that these different orbital parameters align regions of TWLP with regions where the GRS instrument aboard the Mars Odyssey spacecraft detected subsurface water ice [6]. However, they note that the ice may be tens of

centimeters below the surface, which is too deep to be affected by the diurnal thermal wave—hence, no melting would occur. Atmospheric methane may act to increase the surface temperature enough such that zones of TWLP are pushed to high enough latitudes that the ice table is close enough to the surface to feel the effects of daily temperature maxima.

Model: Using a one-dimensional radiative-convective model developed by Pavlov et al. [7], this work will quantify the effects of methane on surface temperature. To date, simulations have been run at values of total Martian surface pressure varying from 5-20 mbar over a range of methane mixing ratios from $1E-10$ to $1E-3$ (see Figure 1). During these runs, water vapor has been held constant at a value of 150 ppm in the lower 25 km and at 2.5 ppm above that, consistent with observational values reported by Rodin et al. [8]. Future work will include allowing water vapor to adjust with temperature, and will thus include the warming effect of increased atmospheric water vapor.

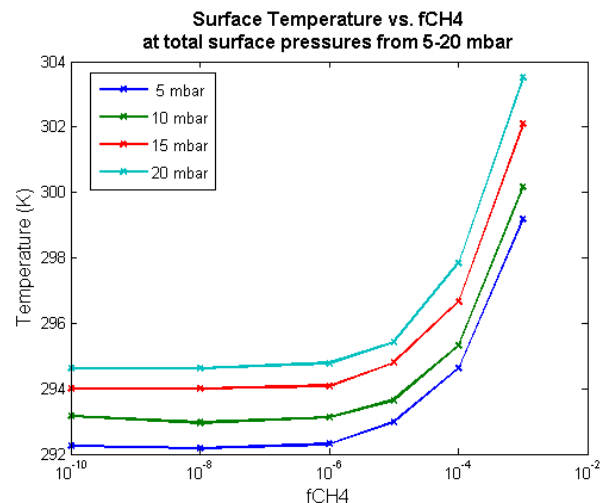


Figure 1. Maximum daily Martian surface temperature is graphed versus methane mixing ratio. The calculations were performed for total surface pressures of 5-20 mbar.

Preliminary Results: The current Martian methane abundance has been measured to be, as a global average, on the order of 10ppb [1-3]. Figure 1 shows that unless the methane mixing ratio (FCH4) is raised to values ≥ 10 ppm (2-3 orders of magnitude greater than any value reported in the literature), the effect of methane alone does not significantly increase surface

temperature. However, as mentioned previously, these values are for the effects of methane alone. If water vapor is allowed to adjust within constraints dictated by Martian temperature and Mars' water inventory, atmospheric methane may act to trigger an increase in atmospheric water vapor, amplifying any temperature increase. This effect could be important to the distribution and extent of areas with TWLP.

Conclusions: The variability of Martian climate is determined largely by orbital parameters such as planetary obliquity and the season of perihelion, and perhaps other factors such as the presence of atmospheric methane. These factors determine whether or not the northern polar regions have ever seen transient liquid water. If liquid water has ever existed, the evidence should be chemically written into the Martian regolith. This signature will be visible to the Phoenix Mars Lander which will provide important ground truth upon landing in 2008.

References: [1] Krasnopolsky V. A. et al. (2004) *Icarus*, 172, 537-547. [2] Formisano V. et al. (2004) *Science*, 306, 1758-1761. [3] Mumma M. J. et al. (2004) *DPS Meeting 36*, abstract 26.02. [4] Richardson M. I. and Mischna M. A. (2005) *JGR*, 110, E03003. [5] Laskar J. et al. (2004) *Icarus*, 170, 343-364. [6] Boynton W. V. et al. (2002) *Science*, 297, 81-85. [7] Pavlov A. A. et al. (2000) *JGR*, 105, 11,981-11,990. [8] Rodin A. V. et al. (1997) *Icarus*, 125, 212-229.

NEAR-PERHELION GLOBAL DUST STORM AND THE STABILITY OF THE PERENNIAL SOUTH POLAR CAP ON MARS. B. P. Bonev^{1,2}, P. B. James³, G. B. Hansen⁴, D. A. Glenar², and J. E. Bjorkman⁴, ¹Solar System Exploration Division, Code 693, NASA Goddard Space Flight Center, Greenbelt, MD 20771 (bbonev@ssdmail.gsfc.nasa.gov), ²Department of Physics, The Catholic University of America, Washington, D.C., 20064, ³Space Science Institute, Boulder, CO 80301, ⁴Department of Earth and Space Science, University of Washington, Seattle, WA 98195. ⁵Ritter Astrophysical Research Center, Department of Physics and Astronomy, The University of Toledo, Toledo, OH 43606.

Motivation: It is uncertain whether the residual (perennial) south polar cap on Mars is a transitory or a permanent feature in the current Martian climate. While there is no firm evidence for complete disappearance of the cap in the past, clearly observable changes have been documented. In particular, observations suggest that the perennial cap lost more CO₂ material in the spring / summer season prior to the Mariner 9 mission than in the corresponding seasons monitored by Viking and Mars Global Surveyor (Figure 1). In this paper we examine one process that may contribute to these changes - the radiative effects of a planet encircling dust storm that starts during late Martian southern spring on the stability of the perennial south polar cap. Our approach is to model radiative transfer through a dusty planetary atmosphere bounded by a sublimating CO₂ surface.

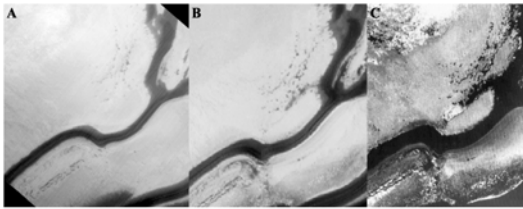


Figure 1

Images of the same region from the perennial south polar cap (lat. $\sim -86^\circ.5$, long. $\sim 0^\circ$ for the fork-shaped region) taken during later summer at near identical L_s and spatial resolution of about 200 meter; (A) Mars Global Surveyor, 2000; (B) Viking, 1977, and (C) Mariner 9, 1972 (the images are credit to NASA).

Radiative transfer model and input parameters:

Our algorithm has been described in [1]. We employed the non-iterative Monte Carlo radiative equilibrium code of Bjorkman and Wood [2] initially developed for astrophysical applications and adapted for the case of a plane-parallel dusty planetary atmosphere. Although this model atmosphere is one-dimensional, the radiation transfer code is three-dimensional and includes wavelength-dependent dust opacity, anisotropic scattering, and thermal dust emission. The “altitude” variable in this algorithm is the local vertical dust optical depth at 550 nm, measured from the top of the atmosphere (τ_{550}).

The most important radiative effects in our simulations are (1) the redistribution, from visible to infrared wavelengths, of energy reaching the surface due to absorption and re-emission by atmospheric dust, and (2) the surface absorption over a wide frequency range. The input parameters needed for modeling these two effects are the absorption and single scattering properties of Martian aerosols and the surface CO₂ albedo spectra. Both of these parameters have been constrained from observations covering multiple spectral regions.

Wavelength-dependent dust absorption and single scattering properties (albedo, absorptive opacity) have been

adopted from studies by Wolff and Clancy [3] and Clancy et al. [4]. These properties are the result of combining previous work in the visible and infrared with subsequent analysis of TES spectra over a wide range of aerosol loading conditions. For dust scattering, we adopted the phase function of Tomasko et al. [5] at 965 nm for the visible and a Henyey-Greenstein phase function with a frequency-dependent value of the asymmetry parameter for the IR.

Polar surface albedo spectra: The total downward flux incident on the surface at each wavelength is partitioned into reflected and absorbed components, depending on the surface albedo. The surface sublimation flux (in energy units) is then given by the difference between the frequency integrated fluxes absorbed and thermally emitted by the surface. Our dusty model atmosphere is bounded by a sublimating CO₂ surface at ~ 147 K.

A very important, but somewhat uncertain, model parameter is the strongly wavelength-dependent surface albedo, that determines how the surface would “respond” to the visible-to-infrared frequency redistribution (by atmospheric dust) of the flux incident on it. For modeling surface albedo spectra we utilized the model described by Hansen [6]. The main advantage of Hansen’s approach is that it has successfully reproduced a wide range of Mars polar albedo spectra measured with different instruments and at different wavelengths [6, 7, 8]. We emphasize that for the purpose of describing the polar surface energy balance, we are interested in the radiative (versus micro-physical) properties of the frost.

Hansen’s model has three free parameters which are constrained by observations, namely: CO₂ “scattering length”, amount of dust intermixed in the frost, and amount of H₂O intermixed in the frost. These parameters were determined from both space-craft and Earth-based observations covering multiple wavelength regimes. In particular we used: (1) PFS/MEX spectra between 2.3 and 4.0 μm [8]; (2) L- and K-band near infrared measurements from SpeX/IRTF [7 and this work]; and (3) visible cap albedos from spectrophotometry with the High Resolution Camera (HRC) on HST [9]. Such multi-wavelength approach is highly desirable, since a single spectral range by itself cannot tightly constrain the three-parameter space for polar surface albedo models.

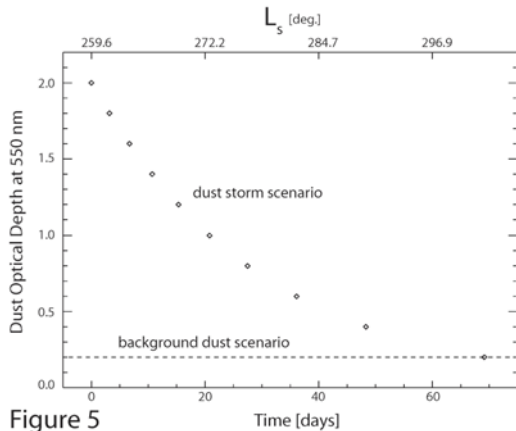


Figure 5

Two scenarios for variation of atmospheric dust optical depth at 550 nm with time used to simulate the effect of a near-perihelion planet-encircling dust storm on the residual south polar cap stability.

Numerical simulations: In order to model the effect of a near-perihelion global dust storm, we assumed that the optical depth over the perennial SPC could be represented in time as an abrupt jump from a background opacity level of $\tau_{550} = 0.2$ to $\tau_{550} = 2.0$ at onset (τ_{550} is the dust optical depth at 550 nm). This increase in optical depth at $L_S \approx 260^\circ$ is followed by an exponential decay to pre-dust storm levels at $L_S \approx 300^\circ$, similar to the observed time scale of the event in 1971.

For series of plausible surface albedo spectrum shown we calculated the variation in sublimation flux with L_S for two modeling scenarios:

1. A “*Global dust storm*” scenario in which the change in sublimation flux is governed by the variable atmospheric opacity and by variable insolation conditions.
2. A “*Background dust*” scenario, in which the dust optical depth is assumed to be constant ($\tau_{550} = 0.2$) throughout the simulation, so that changes in sublimation flux are solely insolation-driven.

These two scenarios are presented in Figure 2 which shows the variation of dust optical depth with time, assumed in our Monte Carlo simulations.

Results: In our actual presentation we will show the deduced variations of the CO_2 sublimation flux with L_S under both scenarios for the variety of polar surface albedo spectra. Here, on Figure 3, we show one representative example. Our main result is that for plausible polar surface albedos the sublimation fluxes are notably enhanced in the global dust storm scenario compared to that of constant background dust. This agrees with the observations of an advanced recession of the residual cap observed after the 1971 near-perihelion dust storm compared to later “non-dusty” years (Figure 1).

Discussion: The enhanced sublimation in the “*dust storm*” scenario is a consequence of (1) significantly increased thermal infrared flux incident on the surface, and (2) the fact that visibly bright surfaces are overall more absorptive at infrared wavelengths. We will discuss these effects in more detail.

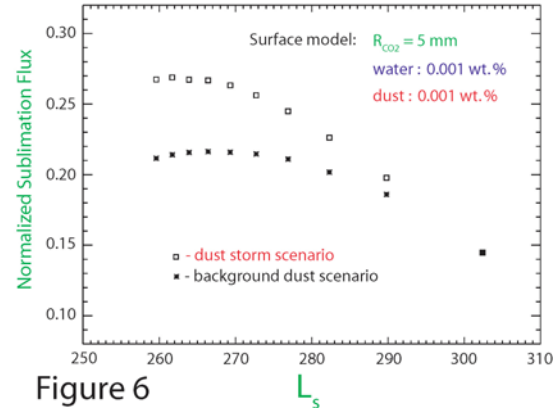


Figure 6

Sublimation flux versus L_S for modeled surface albedo spectrum characterized by scattering length (R_{CO_2}) of 5 mm; intermixed water content – 0.001 wt%; and intermixed dust content – 0.001 wt%. The sublimation flux is normalized to the flux incident to the top of the atmosphere for the point near $L_S \sim 302^\circ$ where the two curves converge.

In addition we will present estimates of the net loss of solid CO_2 during the “*dust storm*” scenario, compared to the “*background dust scenario*”.

Finally we will present two positive feedback mechanisms from a dust storm scenario, that can further enhance sublimation:

1. Dust deposited on the surface as a result of planet-encircling storm could increase the surface absorption and hence the sublimation flux. Because the visible albedo is very sensitive to the dust-to-ice mixing ratio, a small change in this parameter, results in considerable change in surface absorption, and ultimately – increased sublimation rate. The effect of increased surface dust will be illustrated quantitatively.

2. Enhanced sublimation of CO_2 might leave a lag deposit of water ice that will accumulate into a near surface layer of H_2O . Exposed H_2O ice could also contribute to inter-annual variability by increasing the thermal inertia of the surface, thereby delaying seasonal CO_2 re-deposition until the water layer completely sublimates.

Acknowledgements: The authors thank M. J. Wolff for providing a set of single scattering properties of Martian dust, D. Blaney and G. Bjoraker for their assistance with the SpeX/IRTF observations. Modeling CO_2 sublimation fluxes under dust storm condition was supported by a grant from the Mars Data Analysis Program to P.B.J. The near-IR SpeX observations and data analysis were supported by a grant from the NASA Planetary Astronomy Program to D. A. G.

References: [1] Bonev, B. P. et al. (2002) *GRL*, 29, 2017. [2] Bjorkman, J. E. & Wood, K. (2001) *ApJ*, 554, 615. [3] Wolff, M. J., & Clancy, R. T. (2003) *JGR* 108(E9), 5097. [4] Clancy, R. T. et al. (2003) *JGR* 108 (E9), 5098. [5] Tomasko, M. G. et al. (1999) *JGR*, 104, 8987-9007. [6] Hansen, G. (1999) *JGR*, 104, 16471-16486. [7] Glenar, D. H. et al. (2005) *Icarus* 174, 600-603. [8] Hansen, G. et al. (2005) *Planet. Space. Sci.*, 53, 1089-1095. [9] James et al. (2005), *Icarus* 174, 596-599.

USING SILICON AND HYDROGEN GAMMA RAYS FOR THE SIMULTANEOUS DETERMINATION OF DRY-LAYER THICKNESS AND SUB-SURFACE ICE CONTENT IN THE POLAR REGIONS OF MARS. W. V. Boynton, D. M. Janes, M. Finch, and R. M. S. Williams, Department of Planetary Sciences, University of Arizona, Tucson AZ 85721 (wboynton@LPL.Arizona.edu)

Introduction: The 2001 Mars Odyssey Gamma-Ray Spectrometer (GRS) [1] has been a very useful instrument for estimating the amount of sub-surface ice in the polar regions. In our first preliminary look at ice content in these regions [2], we modeled the surface with two layers: a dry layer containing small amounts of H₂O over an ice-rich layer with a variable ice content. We used a plot of the fluxes of epithermal neutrons vs. thermal neutrons and a plot of H gamma-rays vs. thermal neutrons to estimate both the ice content in the sub-surface layer as well as the thickness of the dry layer in the south polar region. This analysis gave a result consistent with an ice content around 35% by mass, and a dry-layer thickness (DLT) of about 40 g/cm². This interpretation was based on some assumptions concerning a “ground truth” H₂O content in the lower latitudes, and we have since shown our assumed H₂O content was lower than the “true” value found by the GRS after a proper calibration. We recognized this potential problem at the time, and stated that the assumption, if incorrect, would yield a lower-limit to the ice content.

With a better calibration, we have been able to revise our estimates of ice content and depth, and indeed the ice content did go up from our original estimates. Currently we feel we have a solid calibration of the gamma-ray data and have limited our analyses to these data. We have previously shown, based on the flux of H gamma rays, that the DLT cannot be more than about 25 g/cm² over most of both polar regions [3]. (The GRS data reduction returns thickness expressed in terms of g/cm². It is a measure of column density which is the parameter to which the measurement is sensitive. Linear depth can be estimated by dividing by an assumed density for this upper surface of the regolith.)

This limit was set by assuming the buried ice was 100% H₂O. Similarly, we showed that the H₂O content of the ice-rich soil cannot be any less than about 30% H₂O by assuming the DLT = 0, i.e. the ice-rich soil is not buried at all. If we use only the H gamma-ray flux, we have only one equation for the two unknowns of ice-content and DLT. We have shown that the flux of Si capture gamma rays provides another equation to address the issue [4] (see figure 1).

Approach: In this work we extend the previous work to take into account another important variable.

This variable is the total macroscopic thermal-neutron cross section of the H-free model soil. The data in figure 1 show the relationship between H and Si fluxes and the DLT and the H₂O content of the sub-surface layer. These calculations are only valid for a particular composition of the dry (H₂O-free) soil. Different amounts of Fe and Cl, both of which are strong absorbers of thermal neutrons (the excitation source of these gamma rays), can change the locations of the points. Higher amounts of these elements will lower the Si flux for otherwise identical H₂O contents and DLT values.

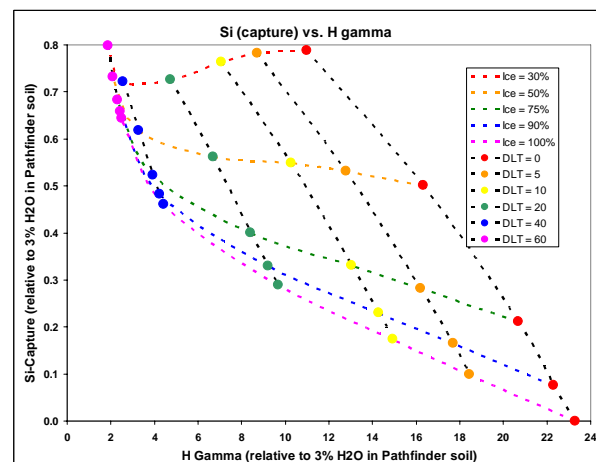


Figure 1. Plot of calculated values of Si and H flux (relative to our standard soil containing 3% H₂O). DLT is the dry layer thickness in g/cm² and the ice content refers to the total H₂O content of the sub-surface ice-rich layer. This array is calculated for a soil which is relatively low in Fe and Cl, two elements which significantly absorb thermal neutrons. A similar array for a high-Fe high-Cl soil plots with Si fluxes significantly lower. To use these calculated model results, one plots the observed flux of the H gamma ray and the Si gamma ray at any given location in the polar region and determines both the thickness of dry layer and the H₂O content of the lower layer by interpolation.

Results: We have now extended the calculations to allow for differences in observed Fe and Cl content in the polar regions. We have calculated many different examples of layered model soils with DLT and H₂O contents similar to those shown in figure 1 but with a range of different Fe and Cl contents. In each of these models, we assume the composition of the soil in

each of the two layers is identical except for the H_2O content. The different H_2O -free compositions can be characterized by a parameter proportional to the total macroscopic thermal neutron capture cross section, and we then plot our results as a 3-dimensional volume relating the total cross section, the H gamma flux, and the Si gamma flux.

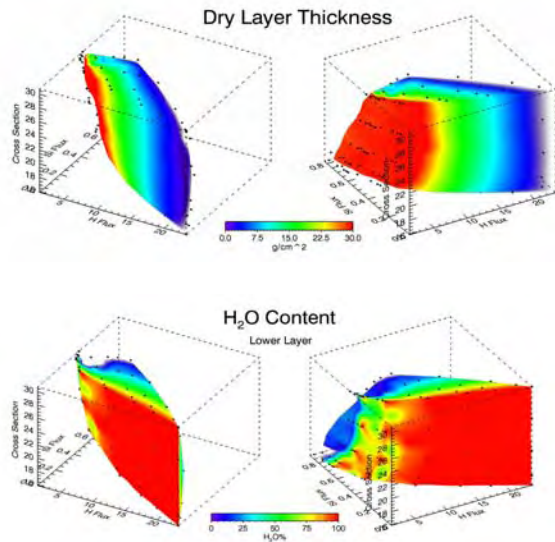


Figure 2. Different views of 3-d plot of calculated fluxes of H and Si gamma rays as a function of different 2-layer models. The models differ in the H_2O content of an ice-rich lower layer, the thickness of the dry layer above it, and a parameter related to the total macroscopic thermal neutron cross section of the dry soil.

In figure 2 we show a graphical representation of the results of these model calculations. The observed Fe and Cl content and the H and Si gamma-ray fluxes of the polar region are used with these model calculations to determine both the H_2O content in the lower layer and the thickness of the dry layer on top. (In these calculations the H_2O content of the upper layer is assumed to be 5%, but the results are not strongly dependent on this value.)

Over most of both the north and south polar regions (Figure 3), the dry-layer thickness is similar, in the range of 0 to 12 g/cm^2 with a 1-sigma uncertainty ranging from 2 to 7 g/cm^2 over most of the region. (The uncertainty is dependent on the statistical uncertainty in the Fe and Cl content and the H and Si fluxes; it does not include model uncertainties.) The H_2O content of the ice-rich layer differs between the two poles with the south having the greater H_2O content. Values in the south range from about 35% to 75% H_2O . In the north, the values range from about 35% to 50%. The uncertainties on these values are larger in the south, ranging from about 10% to 16% H_2O over most of the

south and 6% to 10% H_2O over most of the north. (The uncertainties at lower latitudes where the signal is weaker is generally higher than that given above.)

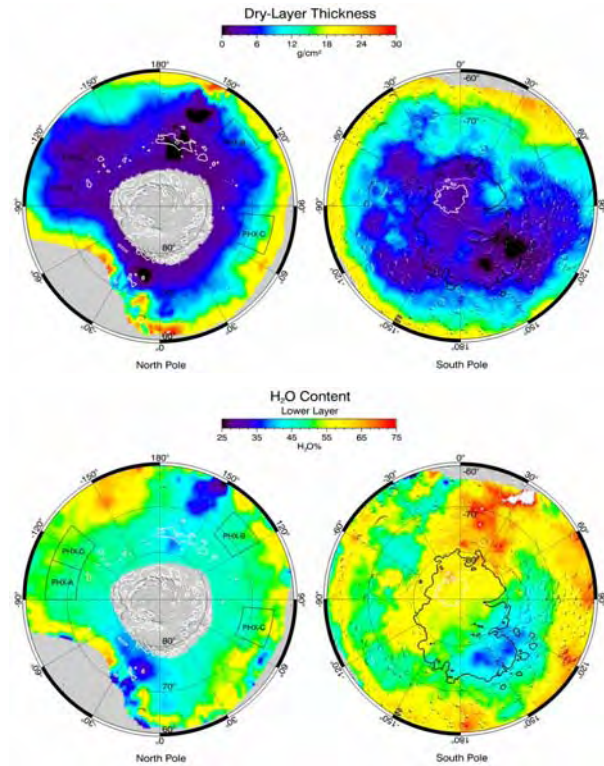


Figure 3. Maps of the polar region showing variations in dry-layer thickness (DLT) and H_2O content of the lower layer. Regions around the north polar residual cap, where the spatial resolution of the GRS does not permit a clear determination of the surrounding areas, has been masked out. Similarly, the areas at lower latitudes where the presumed ice level is deep are also masked out. The residual caps are outlined in white and south polar layered terrain is outlined in black.

Discussion: The differences in H_2O content between the north and south may be an indicator of differences in the accumulation rates of snow and dust in the two hemispheres when the ice-rich layers were deposited. The thickness of the dry layer is probably more indicative of current conditions rather than conditions in the past when the ice was deposited. These points will be discussed at the meeting.

References:

- [1] Boynton *et al.* (2004) *Space Sci Rev.* 110, 37-83.
- [2] Boynton *et al.* (2002) *Science*, 297, 81-85.
- [3] Boynton *et al.* (2004) *6th Intl. Conf. on Mars*, Abstract #3259.
- [4] Boynton *et al.* (2005) *LPS XXXVI Abstract* #2154.

LANDSCAPE EVOLUTION AND THE REINCARNATION OF THE SOUTHERN RESIDUAL ICE CAP.

S. Byrne¹ and M.T. Zuber², ¹Lunar and Planetary Laboratory, University of Arizona, Tucson, Arizona, USA (shane@lpl.arizona.edu), ²Earth, Atmospheric and Planetary Science, Massachusetts Institute of Technology, Cambridge, Massachusetts, USA.

Introduction: Recent observations conducted with the Mars Orbiter Camera (MOC) have revealed the southern residual CO₂ cap to contain a wide range of landforms [1]. Among the most interesting and populous are flat-floored quasi-circular pits with steep walls (Figure 1), which have been dubbed Swiss-cheese features. Interannual comparisons [2, 3] show that two separate classes of these depressions are expanding laterally at rates of ~2m/yr and ~4m/yr. Modeling of the evolution and growth of these depressions by [4] allowed them to infer an involatile basement layer and place a small upper limit on the total volume of CO₂ in the cap. Hyper-spectral and neutron spectrometer data [5, 6] also suggest a thin CO₂ covering.

Analysis of the size distribution of a subset of these features [7] combined with the newly published expansion rates of [3] suggest they all have similar ages and may be as young as ~22 Martian years. This age would coincide with the global dust storm of 1971. The residual CO₂ ice cap contains layers roughly 2m thick [1]. Each layer represents some accumulation episode in the recent past. Changes in the appearance of the residual ice between the Mariner 9 and Viking missions [8] indicate that the top-most layer was deposited in that time-frame, soon after the global dust storm of 1971. Thus, it appears likely that some kind of historical record of climatic events (such as the 1971 global dust storm) exists both within the stratigraphy and landforms of the south polar residual cap.

The spatial density of the Swiss-cheese features and the rate at which they expand mean that it is unlikely that any part of the residual ice cap is older than a few centuries. *Given this, we may ask (without appealing to extraordinary luck): how can there be a residual cap present today for us to observe?*

To try and answer this and other questions. We have developed a model to examine the evolution of a CO₂ ice landscape at arbitrary latitude. This model reproduces the morphologies and expansion rates seen in the actual residual CO₂ ice cap.

Model Description: Energy drives the evolution of these features. On this CO₂ surface, sublimation lasts through most of the summer until the insolation falls below the emitted radiation allowing the ice to cool below the equilibrium temperature and drive condensation, which lasts throughout the winter. Several factors influence how much energy a given surface element (facet) will absorb/emit including the

slope/aspect of the surface, absorption of energy reflected from other surface elements, shadowing by other surface elements and atmospherically contributed radiation. Should the water ice substrate be uncovered it may also change temperature and store thermal energy in the subsurface.

Such computations for an arbitrary landscape take too long to produce useful results. Analytic solutions may be applied in a very restricted set of geometries [4]; however, we wish to make progress on the general case. The assumption we will make which enables this work is that *each CO₂ facet behaves as if it were surrounded by an infinite flat plain*. Under this assumption facets may shadow themselves, but are not shadowed by adjacent topography and we can analytically calculate the incident shortwave and long-wave energy from the surrounding plain.

Comparisons of this model with the slower, more-complete calculations will be presented to show that the errors introduced by our assumptions are not especially egregious.

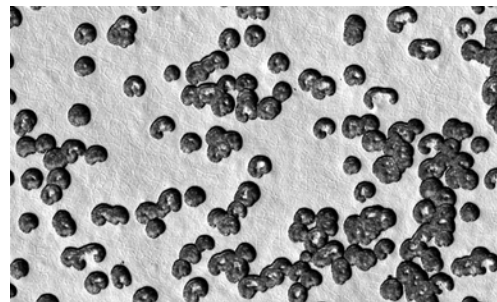


Figure 1: Swiss-cheese pits (dark-floored features) expand several meters per year and are slowly consuming the 8m thick slab in which they are embedded.

Results: With the model described above we can begin to ask interesting questions such as: what is the fate of the current residual ice deposit? as well as why do we observe a residual ice deposit at all if it is being so rapidly eroded?

The fate of our model surfaces is controlled by their surface roughness. Using these model assumptions, surface roughness always increases with time, which results in an unstable situation. When the surface roughness exceeds a critical point small pits can begin to develop. The walls of these pits rapidly steepen and begin retreating which enlarges and deepens the pit.

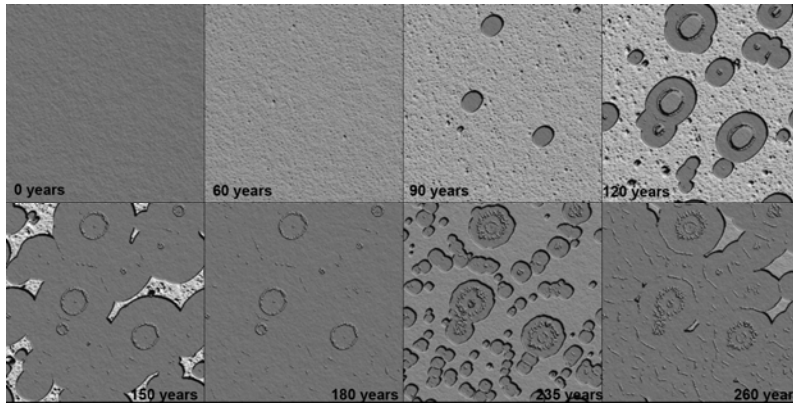


Figure 2: Results of sample model run, showing shaded relief of model topography at 0, 30, 60, 90, 120, 150, 180, 235 and 260 Martian years. Dashed lines in figure 3 correspond to these model times. Illumination from the upper right, see text for discussion.

Soon these pits reach the involatile basement beneath the CO₂ ice slab; this continued expansion rapidly consumes the original CO₂ slab. This situation always occurs even if the surface of the CO₂ slab has a high enough albedo to have a net mass gain each year.

A typical example is shown in the first 6 frames of figure 2. The surface remains stable for many Martian decades (the duration of this phase is linked to the roughness of the initial surface). Once Swiss-cheese features are initiated they quickly consume the CO₂ slab. Small isolated remnants of CO₂ ice survive by falling into a regime where ablation from their north sides is balanced by condensation on their south sides.

This presents a problem. It seems implausibly fortunate that we would happen to observe such a transient event on Mars today. Once the underlying water ice is exposed, it will not frost over again if Mars were to repeat like clockwork every year [4, 9].

To resolve this we adjust the model so that a few centimeters of fresh CO₂ are dumped instantaneously on the residual cap every few decades. Such a situation is not unlikely, we have indications that extensive deposition occurred after the 1971 dust storm [8]. Once covered with CO₂ ice, the cap can then begin accumulating mass and growing in thickness again. This continues until the surface roughness again exceeds a stable state and the process repeats itself (last two panels of figure 2). Interestingly the position of the Swiss-cheese features on this cap is controlled by where the isolated remnants of the previous cap are located. Figure 3 shows how the volume of ice (scaled up to the entire cap area) varies with time. One can see several incarnations of the residual cap grow and be consumed by Swiss-cheese. In this model run, the surface roughness of the freshly deposited layer adds to the roughness of the sub-CO₂ basement which means that each successive residual cap incarnation

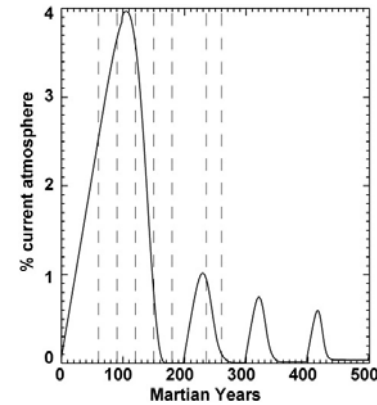


Figure 3: Variation in the volume of the cap for the model run in figure 2. Here, we assume the model domain is representative of all cap locations.

survives for a shorter period than the last. Situations where this is not the case, and successive residual-cap incarnations are of similar size, can also be created. Variations in residual cap extent (not included here) may also exist and affect the total cap volume.

We conclude that interannual climatic variability is actually a requirement for the continued existence of a residual CO₂ ice cap. The cap is not 'stable' in the usual sense of the word, but instead is constantly being destroyed and recreated. The deposition of fresh ice reported by [8] may be linked to the large dust-storm which occurred in 1971. Such dust storms are confined to southern summer and so, due to this seasonal timing, may only be capable of dumping excess CO₂ on the southern cap. It is unknown why the residual CO₂ cap is at the southern pole while the northern pole (which is more thermodynamically stable due to its lower elevation) is CO₂-free during the summer. These results indicate that it may be the timing of the dust-storm season which determines which pole maintains a residual CO₂ ice cap.

We will report on this surface modeling which reproduces other morphologies within the residual cap. We will present a historical model based on combining our modeling with the feature sizes and ablation rates found within the present residual ice cap. We will post these cap evolution models as movies at: <http://www.gps.caltech.edu/~shane/src/landscape/>.

References: [1] Thomas et al., *Nature*, 404, 161–164, 2000. [2] Malin et al., *Science*, 294, 2146–2148, 2001. [3] Thomas et al., *Icarus*, 174(2), 535–559, 2005. [4] Byrne and Ingersoll, *Science*, 299, 1051–1053, 2003. [5] Bibring et al., *Nature*, 428, 627–630, 2004. [6] Tokar et al., *GRL*, 30(13), 2003. [7] Byrne and Ingersoll, *GRL*, 30(13), 2003. [8] James et al., *JGR*, 84, 2889–2922, 1979. [9] Jakosky and Haberle, *JGR*, 95, 1359–1365.

A FIELD DEMONSTRATION OF THERMAL DRILLING TECHNOLOGY FOR THE CHRONOS SCOUT 2011 MISSION. Greg Cardell^{1,2}, Miles Smith^{1,3}, Michael Hecht¹, Robert Kowalczyk¹, Claus Mogensen¹, Alberto Behar¹. ¹Jet Propulsion Laboratory, 4800 Oak Grove Drive, Pasadena CA 91109, [2greg.cardell@jpl.nasa.gov](mailto:greg.cardell@jpl.nasa.gov), [3miles.smith@jpl.nasa.gov](mailto:miles.smith@jpl.nasa.gov)

Introduction: The Chronos Scout mission is proposed to launch in August of 2011, coinciding with the 100th anniversary of Amundsen's departure to the South Pole. Chronos will follow a type IV trajectory Mars, where it will deliver a pair of thermal drills to the North polar cap. With the goal of unlocking the secrets of the past Martian climate, the drills will tunnel through the ice in search of water isotope variations, dust layering, and other climate markers. The drills will each carry a sideways-looking camera to capture images of strata, while meltwater generated by the drills will be delivered through a heated tether to *in situ* instruments at the surface. We present results from a field test of the Chronos thermal drilling technology.

Thermal Drilling: On Earth, conventional coring techniques provide access to climate markers, such as the isotope ratios HDO/H₂O and H₂¹⁸O/ H₂O. However, these techniques require heavy drilling equipment, transport and handling of ice cores, and do not lend themselves to automation or to *in situ* analysis. In contrast, thermal drilling uses resistive heating to melt through the ice, with the resulting water being pumped to the surface so that the borehole remains dry. This approach requires less power, is simpler, more compact and, because the sample is liquid, the drill can readily be interfaced with surface instruments that provide *in situ* analysis of water chemistry, isotopic ratios, and dust content. In this way, thermal drilling is also the ideal choice for exploration of planetary ice.

Site Selection: A number of terrestrial analog sites were considered for the Chronos field demonstration. Selection criteria were: (1) An ice temperature significantly colder than freezing, to provide a test under the same order of magnitude conditions as will be met on Mars, (2) A firn-ice transition that is shallow enough so that a 100 meter penetration will include significant testing in solid ice, and (3) Available logistical support. The NSF camp at the Greenland summit, with its relatively cold ice (~30 °C) and modest firn depth (~60 m), meets all three criteria and was selected as the field site, with deployment scheduled for July 2006.

Field Test Description: Field-testing endeavors to simulate a maximum number of components of the Chronos mission. These include:

- The deployment of two thermal drills at the Summit site, each fully instrumented with a

camera for examining strata, temperature sensors for measuring thermal gradient, and an array of engineering sensors for examining the health of the drill.

- The testing of a tether that provides transport of meltwater to the surface through a heated Teflon tube and flexible aerogel insulation, as well as providing down-hole power and RS-422 data transfer between the drills and a surface computer.
- Operation of a deployment mechanism that releases the tether in a controlled manner, while measuring the depth of the drill and the down-hole tether tension.
- Testing of software for the full automation of the drill, switching of the tether heater, and control of the deployment hardware.
- The collection of meaningful scientific data with in-line, *in situ* analysis of the water sample. This surface instrument package includes a water isotope analyzer from Los Gatos Research Inc., for measuring HDO/H₂O and H₂¹⁸O/ H₂O, a flow-through particle counter for counting and sizing of suspended dust, and water conductivity, pH, and dissolved oxygen sensors.

The primary objective of these tests is to show that Chronos can not only meet the science goal of reconstructing the past Martian climate, but will also answer the technology challenges of such a mission.

MONITORING AND PHYSICAL CHARACTERIZATION OF THE SOUTH SEASONAL CAP OF MARS FROM OMEGA OBSERVATIONS. S. Douté¹, Y. Langevin², F. Schmidt¹, B. Schmitt¹, M. Vincendon², J. P. Bibring², F. Poulet², E. Deforas¹, B. Gondet², ¹*Laboratoire de Planétologie de Grenoble Bât D de Physique B.P. 53 Grenoble Cedex 09 France sylvain.doute@obs.ujf-grenoble.fr*, ²*Institut d'Astrophysique Spatiale, CNRS / Université Paris XI, Orsay Campus, 91405, France.*

Introduction The time and space evolution of the South Seasonal Polar Cap (SSPC) is a major annual climatic signal. The composition, physical state and texture of the SSPC give clues about the exchange of CO₂, H₂O and dust with the atmosphere. The recession of the SSPC was observed recently: (i) from earth in the visible range with HST [1], or from MGS spacecraft with MOC images [2], (ii) in the thermal IR range by the TES [3] (iii) by changes in topography revealed by MOLA [4] and with HEND/MO measurements [5]. The imaging spectrometer OMEGA on board Mars Express has acquired the most comprehensive set of observations to date in the near-infrared (0.93-5.1 microns) on the recession of the SSPC from mid winter (Ls=130°, December 2004) to early summer (Ls=290°, November 2005) [Langevin et al., this conf.]. The time resolution is 3 days to one month and the spatial resolution ranges from 2 to 10 km/pixel. The spectral range covered by OMEGA is particularly relevant for our studies since it samples numerous absorption bands distinctive of CO₂ and H₂O in their solid state. Here we analyze OMEGA spectral images to (i) determine the contour (i.e. crocus line) versus time of the SSPC (ii) segment the latter into different icy terrains and (iii) obtain their physical properties with unprecedented accuracy.

Methods *Detection of CO₂, H₂O, and dust* We use a supervised automatic classification method, called "wavanglet", that identifies spectral features in wavelet sub-spaces to detect reference compounds [6]. We evaluated the sensitivity of wavanglet for the detection of CO₂ and H₂O ices as a function of certain physical (e.g. grain sizes) as well as geometrical parameters (e.g. solar incidence angle) using synthetic data and real OMEGA data. "Wavanglet" coupled with statistical techniques (PCA and ICA) applied to the OMEGA images differentiate several types of icy terrains according to their composition and their physical properties (Fig. 1).

Physical characterisation Then we extract the purest spectra of these terrains and model them (see Figure 3) to obtain quantitative values for the physical properties, e.g. abundances, granularity, layer thicknesses. The removal of the spectral effects due to aerosols and atmospheric gases is respectively performed using a 3D multiple scattering Monte-Carlo model and scaling a reference atmospheric transmission spectrum according the estimated gaseous CO₂ column [7]. The modelling of the spectra after atmospheric correction is performed with a radiative transfer algorithm that calculates the spectral reflectance of layered, icy, and dense materials taking into account shadowing effects due to macroscopic roughness [8]. Each layer can have a granular or a compact (icy matrix with inclusions) texture.

Results Figure 1 shows the distribution of CO₂ (blue) and water ice (red) for the time sequence between Ls = 220° and

Ls = 230°.

By definition the crocus line separates the area still mantled by CO₂ from the ice free area (violet). With a series of similar mosaics covering contiguous ranges of Ls, we estimate numerically the latitude of the crocus line according to longitude and time. Figure 2 shows its evolution according to time observed by TES (triangle and diamonds) in 1997 [3] and by OMEGA in 2005 (colour dots) along 3 longitudes: (a) 60°W, (b) 150°W and (c) 240°W. Along longitude 60°W, OMEGA and TES observations are compatible while OMEGA sees a faster recession of the SSPC for the whole time period along longitude b. For longitude c the situation is first similar to the latter case but, after Ls=250°, TES sees a more rapidly disappearing frost than OMEGA does. The discrepancy could be explained by the existence of a geographic mixture of CO₂ ice and ice-free terrains inside both instrument pixels. While the ice would still display significant signatures in the near infrared, the hot ice-free terrains will dominate the TES signal in the infrared.

Before equinox the seasonal cap is mostly composed of a clear slab of CO₂ ice ≈ 30 cm thick, with typically 0.02 to 0.06 % in volume of dust and H₂O ice inclusions (Figure 4, A). Starting at Ls=200-230° the recession of the SSPC becomes longitudinally asymmetric with the appearance of the cryptic region, a cold region with relatively low albedo (Fig. 1 pinkish area inside the SSPC). The modeling shows that, in the latter region, the cover of CO₂ remains continuous although it is reduced in thickness (100 to 150 mm) and is contaminated by dust (up to 7 weight %) and water (up to 0.42%) in a thin upper layer (Figure 4, B and C). The dust contamination accelerates the sublimation of CO₂. By Ls=242°, patches of ice-free terrains appear while the thickness of the CO₂ slab is decreasing and the superficial contamination is dramatically reduced (Figure 4, D). The latter fact is best explained by the dust being swept to low lying area by winds. The regression is much slower for the rest of the cap since the albedo of the CO₂ layer overlying its mineral substratum remains higher. These results strengthen our interpretation of figure 2, especially after Ls=250° for longitude 240°W that cuts the cryptic region.

References

- [1] James, et al., 2005, *Icarus*, **174**, 596.
- [2] Benson, et al., 2005, *Icarus*, **174**, 513.
- [3] Kieffer, H.H., et al., 2000, *J. Geophys. Res.*, **105**(E4), 9653.
- [4] Smith, et al., 2001, *Science*, **294**, 2141.
- [5] Litvak, et al., 2004, *Solar System Research*, **38**, 167.
- [6] Schmidt, F., et al., 2006, *IEEE Transactions on Geoscience and Remote Sensing*, submitted.
- [7] Langevin, et al., 2006, *Nature*, in press.
- [8] Douté, et al., 1998, *J. Geophys. Res.*, **103**(12), 31367.

Seasonal South Cap of Mars

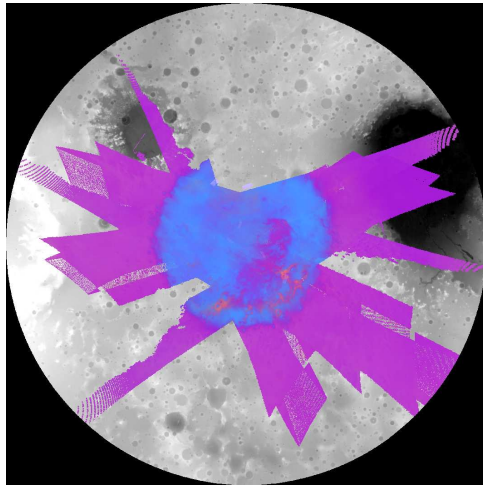


FIG. 1 – Spatial distribution of CO₂ ice, H₂O ice, and dust obtained between L_s = 220° and L_s = 230° using “wvangellet”. Blue : CO₂ice. Red : Water ice. Violet : dust. Background : MOLA topography in south polar stereographic projection until 30° S.

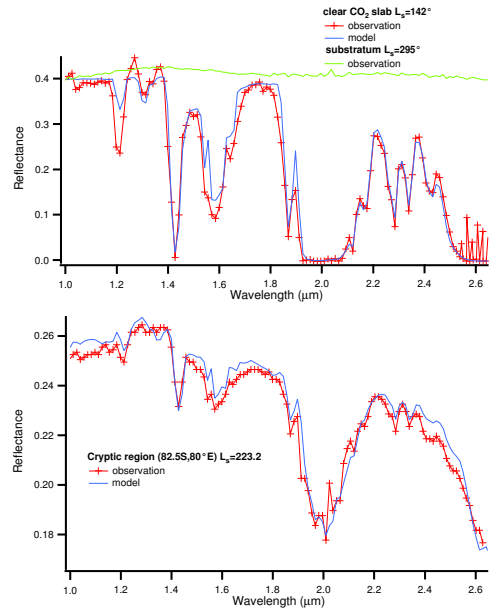


FIG. 3 – Modeling the spectrum of a representative location in the cryptic region of the SSPC at two different L_s. The top and bottom panels corresponds respectively to the situation A and C of Fig. 4. The values retrieved for the main physical parameters concerning CO₂ ice, H₂O ice, and dust are indicated in the main text.

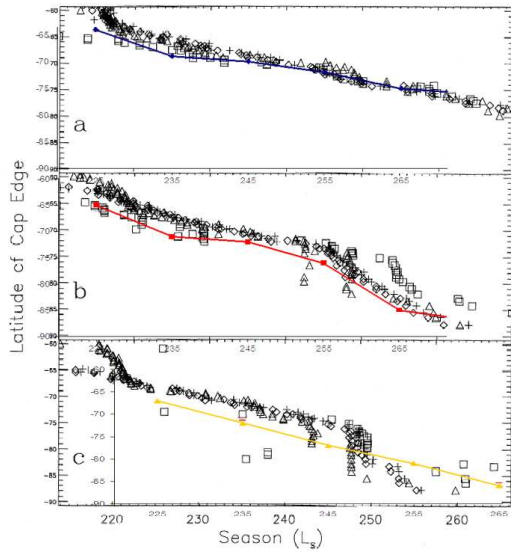


FIG. 2 – Comparison of the SSPC recession observed by OMEGA and TES along longitudes : 55-65° W (a), 145-155° W (b) and 235- 245° W (c). Color dots : OMEGA observations in near IR. Triangle and diamonds : TES data in thermal IR [3]. Square : visible albedo observed by TES [3].

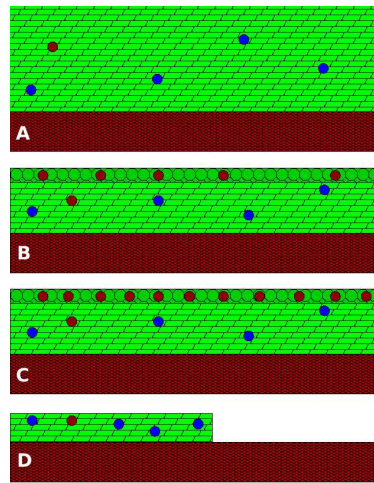


FIG. 4 – Scenario for the evolution of the “cryptic” region from the end of winter to just before the crocus date. The brown, light green and dark green boxes respectively represent the mineral substratum, the “nearly pure” and contaminated CO₂ ice. The little colored disks symbolize dust (brown) and water (blue) inclusions embedded in the ice. The letters refer to the main text.

SIMULATION OF DUST SEDIMENTATION ON THE CALIBRATION TARGETS FOR THE SURFACE STEREO IMAGER ONBOARD THE PHOENIX MARS LANDER 2007, L. Drube¹, M. B. Madsen¹, M. Olsen¹, J. Jørgensen¹, D. Britt², M. Lemmon³, C. Shinohara⁴ and P. Smith⁴, ¹ University of Copenhagen, Denmark (line@fys.ku.dk), ²The University of Central Florida, USA, ³Texas A&M University, USA, ⁴University of Arizona, USA

Introduction: The Phoenix Mars Lander 2007 mission will carry three identical calibration targets to verify and validate the preflight calibration of the Surface Stereo Imager (SSI) and to monitor the stability of this calibration during the mission.

The specially designed calibration targets ('the caltargets') each consist of an aluminum plate with six different color chips each in two sizes and four experimental color chips. The pigments for the first set of chips consist of inorganic pigment material dispersed in silicone RTV material and they are green (chromium oxide), yellow (goethite), blue (cobalt aluminate). The second set of chips is three shades of gray (mixture of titanium dioxide and carbon black, reflectivity: 60%, 40%, 20%).



Fig. 1: The caltarget

Underneath each of the six large color chips a 7 mm tall ring-magnet with an inner diameter of 5 mm and an outer diameter of 11 mm is embedded. These ring-magnets will protect roughly the central 3 mm from magnetic dust settling onto the surface. The design of each individual magnet is almost identical to that of the sweep magnets flown on MER [1]. On MER, using such a sweep magnet it has been possible to maintain a relatively clean surface in the dusty Martian environment (see fig. 2). From the results it seems that almost any airborne particle contains at least a small amount of a strongly paramagnetic phase or a ferrimagnetic phase [1]. We have recognized later that the ferrimagnetic phase is predominantly magnetite [2]. This remarkable property of the Martian

dust is the basis of the idea to have selected chips of pigmented material placed at the centers of the ring-magnets. These color chips constitute a color calibration target. These color chips will almost not be obscured by reddish dust accumulation during the mission.



Fig. 2: Sweep magnet on MER [1]

The six small color chips are exposed to the natural Martian dust environment to allow a comparison with the protected ones. Each of the four experimental color chips has a different surface coating (Au, Pd, Cu and RTV).

In addition to serving as calibration targets for the SSI, these targets serve at the same time as an improved and more sensitive sweep magnet experiments. On the MERs the sweep magnets were embedded in gray aluminum (fig. 2). For Phoenix the sweep magnets in the caltarget will have differently colored chips to enhance the sensitivity for detection of any dust that might be able to enter and settle there. In this way the caltargets will also serve as a repetition of the sweep magnet experiments on another location on the surface of Mars – and with improved sensitivity compared to MER.

Simulation experiments: To test the performance of the caltarget these will be exposed to wind and dust in a simulated Martian atmosphere and pressure in the Mars Simulation Chamber at the University of Aarhus, Denmark. In this facility it has not been possible to observe slow sedimentation of dust from the atmosphere and consequently a less sophisticated 'Dust Sedimentation Chamber' was built at the Niels Bohr Institute, Denmark. It is non-pressurized and has earth atmospheric composition.



Fig. 3: Dust Sedimentation Chamber

Dust will be injected into the chamber near the top by pressurized air (see fig. 4).

Several types of dust have been used in these experiments. The most important dust sample used is from Salten Forest in Denmark, as this material is so far the best magnetic analog to mimic the observed magnetic properties of the dust on Mars. This sample contains hematite, maghemite, goethite and silicates, has a suitable saturation magnetization and a reddish color [3].



Fig. 4: Dust injection outlet

For the caltarget to get exposed only to 'slow' sedimentation we have covered it by protective caps during the dust injection and for a while thereafter. (See fig. 5).



Fig. 5: Protection caps being lifted off the caltarget and a calibration plate for the experiment

For one series of testing we investigated the distribution of minerals and dust particle sizes along a cross section on top of a single magnet. This was done by positioning several 3 mm diameter transmission electron microscope grids (TEM-grids) along the cross section of a magnet. This allows a detailed investigation of material on the calibration surface and for the Salten Forest sample, and the distribution of the different crystal structures across the magnet color chip has been studied.

Results:

A preliminary report of these experiments will be offered at the conference.

References: [1] Bertelsen, P. et al., (2004) /Science/ *305, 827-829. [2] Goetz, W. et al., (2005) /Nature/ *436*, 62-65. [3] Bertelsen, P., (2001), Ph.D. Thesis, Denmark.

A BETTER FLOW LAW FOR DIRTY, VERY SLOW ICE. W. B. Durham¹, A Pathare², L. A. Stern³, and S. H. Kirby³, ¹Dept. of Earth, Atmospheric, and Planetary Sciences, MIT, Cambridge, MA 02139, wbdurham@mit.edu, ²Planetary Science Institute, Tucson, AZ 85719, avp11235@gmail.com; ³U. S. Geological Survey, Menlo Park, CA 94025.

Introduction: Preliminary indications from laboratory experiment have suggested that hard particulates of varying size and composition do not have a profound effect on the steady-state strength of ice I [1]. However, geological strain rates are very much slower than those imposed in most laboratory tests, and can call up deformation physics not normally seen in ordinary lab experiments. The key questions implied in the title are ones we are currently addressing in a new round of lab tests, to wit: (1) what is the effect of hard particles on the deformation of ice in the grain-size-sensitive (GSS) creep regime, and (2) what is the minimum ice content required for soil mobility at very low strain rates? We do not yet have the answers.

Effect of dust in the GSI creep regime: At $T < 250$ K and differential stresses above 1 MPa, the deformation of ice I is dominated by dislocation creep, a grain-size-insensitive (GSI) mechanism. Under these conditions, the effect of particulates is a hardening caused mainly by increased tortuosity of flow paths around particles and viscous drag of flowing ice at particulate surfaces. There is no indication that hardening by pinning dislocations, as in dispersion hardening (see [1]), or by pinning grain boundaries is an important process in ice I at planetary conditions. For the dislocation creep regime, Durham et al [1] found that for ice I mixed with hard particulates at volume fraction $0 \cdot \phi \cdot 0.56$ and $142 \cdot T \cdot 223$ K, the steady-state flow strength σ follows the relationship

$\sigma_{\text{ice I + particulates}} = \sigma_{\text{pure ice}} (\exp(b\phi))$,
where $b \approx 2$. At $\phi = 0.56$ the hardening is roughly a factor of 3 to 4 in σ , or about two orders of magnitude in viscosity for stress exponent $n = 4$ rheology.

Effect of dust in the GSS creep regime: Until recently direct measurements of GSS creep in laboratory ice was unattainable, the breakthrough being the development of techniques for making ice of very small grain size [2,3]. Creep rates in the GSS regime are enhanced by the presence of grain boundaries in the material, which may act as diffusion pathways (Coble creep), planes of weakness (grain boundary sliding), sinks for intracrystalline defects (Nabarro-Herring creep), etc. The dependence of strain rate $\dot{\gamma}$ on grain size d in the GSS creep regime is usually written as

$$\dot{\gamma} \propto d^{-p},$$

where p is a constant usually ≥ 1 . Based on work done at $T > 250$ K, that dust in Martian ice deforming in the GSS creep regime could have a softening or a harden-

ing effect. At warm temperatures, particulate pinning of grain boundaries can soften ice by impeding grain growth, thus retaining creep within the GSS regime [4]. There is also a direct effect of particulates on GSS processes given the possibility that particulates concentrate on grain boundaries under some conditions [4,5], promoting processes such as enhanced grain boundary diffusion [6], and work hardening [7].

Grain growth: We have observed hardening by grain growth in fine-grained ice I near the warm edge of the GSS creep regime, $T > 220$ K [8]. Grain growth tends to occur during GSS creep because GSS mechanisms themselves usually do not generate intracrystalline defects. The same is not true of dislocation creep, the main GSI mechanism we observe in ice, where recrystallization of large grains to small is a common process. Thus the possibility exists, in pure ice at least, that a polycrystalline solid deforming through large strains will approach a grain size such that both GSS and GSI mechanisms contribute to deformation [9].

The rate of grain growth is affected by a number of external factors besides pressure and temperature, such as solutes and insoluble impurities, pores, and the presence of second phases [4,5,10]. In ice at very warm temperatures for example, it has been shown that the presence of particulate impurities at the few percent level has a weakening effect caused by the particle pinning of grain boundaries, preventing grain growth and thus allowing GSS mechanisms to operate at high rates [4]. Similar effects may occur in terrestrial ice caps [10]. It is reasonable to suspect a similar effect at Martian temperatures, but the conjecture has not been tested in the laboratory.

Minimum mobility: It is of great relevance to determine the minimum concentration of ice in Martian soils that is required to degrade soil strength. Such knowledge may provide a useful constraint on the ice content of "softened" high-latitude terrains. At high particle fractions, the rigid framework formed by particle-particle contacts gives soil a very high strength, so lab testing can again be problematic because of strain-rate scaling issues. Higher differential stresses must be applied in the lab, which moves the deformation regime closer to the brittle-ductile transition. This represents a rather fundamental change in deformation mechanism, with a strong shift in the dependence of viscosity on temperature, pressure, and strain rate. Conservative application of the so-called Goetze rule

[11], that differential stresses must not exceed confining pressure in order to assure ductility, is strongly recommended for experiments. A partially brittle deformation mechanism in the lab will extrapolate to an incorrectly low viscosity for Martian surface materials.

Great care must be taken, therefore, to properly identify the deformation mechanism at work in the lab. The brittle-ductile transition in all rocks, including ice + rock mixtures, is gradual, with cataclastic fracturing and crushing of grains as one end member behavior and fracture-free flow of the matrix material as the other. In the case of ice mixtures, pressure melting also has been implicated [12,13].

The direct approach of measuring stress vs. strain rate well outside the brittle field is unlikely to succeed. The required strain rates will be nearly geological. Studies of ice + sand deformation at high sand fraction, with both planetary and terrestrial frozen soil (permafrost) application, show behavior that is either demonstrably brittle or too close for comfort [12-14]. Most testing like this is carried out at high temperatures in an effort to maximize ductility, although the special characteristics of water-ice deformation near the melting point also suggest a different mechanism [15].

References: [1] Durham W. B. et al. (1992) *JGR.*, 97, 20883-20897, 1992. [2] Goldsby D. L. and Kohlstedt D. L. (1997) *Scripta Mater.*, 37, 1399-1406. [3] Stern L. A. et al. (1997) *J. Geophys. Res.*, 102, 5313-5325. [4] Baker, R. W. and Gerberich W. W. (1979) *J. Glaciol.*, 24, 179-194. [5] Alley R. B. et al. (1986) *J. Glaciol.*, 32, 425-433. [6] Bruhn D. F. et al. (1999) *JGR*, 104 (B1), 707-724. [7] Dresen G. et al. (1998) *GRL*, 25, 1245-1248. [8] Durham W. B. et al. (2001) *JGR*, 106, 11031-11042. [9] de Bresser J. H. P. et al. (1998) *GRL*, 25, 3457-3460. [10] Thorsteinsson, T. et al. (1999) *J. Glaciol.*, 45, 338-345. [11] Evans, B. and Kohlstedt D. L. (1995) in *Rock Physics and Phase Relations: A Handbook of Physical Constants*, Ref. Shelf Vol. 3, ed. by T. J. Ahrens, pp. 148-165, AGU, Washington, DC. [12] Ma W. et al. (1999) *Cold Regions Sci. and Technol.*, 29, 1-7. [13] Mangold N. et al. (2002) *Planet. Space Sci.*, 50 (4), 385-401. [14] Parameswaran V. R., and S. J. Jones (1981) *J. Glaciol.*, 27, 147-155. [15] Dash J. G. et al. (1995) *Rep. Prog. Phys.*, 58, 115-67.

EFFECT OF A SURFACE COVER OF DUST ON SUBLIMATION RATES IN THE POLAR LAYERED DEPOSITS ON MARS. M.D. Ellehøj¹ and C.S. Hvidberg¹. ¹Niels Bohr Institute, University of Copenhagen, Juliane Maries Vej 30, 2100 Copenhagen Ø, Denmark. ellehoj@gfy.ku.dk, ch@gfy.ku.dk

Introduction: The permanent polar caps on Mars contain the largest known reservoir of H₂O ice, and are important factors in the global water cycle. The polar layered deposits loose H₂O to the atmosphere by sublimation during the summer period. The H₂O remain in the atmosphere and is transported by the wind until it condenses out during colder periods. This has been observed by Mars Global Surveyor Thermal Emission Spectrometer (TES) [1].

Both permanent polar caps consist mainly of H₂O ice [2, 3]. In the winter season, CO₂ condenses out of the atmosphere and creates a seasonal surface layer of CO₂ ice in the high latitudes [4]. On the north polar layered deposits, this layer disappears during the summer season, when the temperature rises above the CO₂ sublimation temperature, and thereby the H₂O ice in the permanent polar cap is exposed at the surface (figure 1). On the south polar layered deposits (figure 2), there exists a small region with a permanent layer of CO₂ ice exposed on the surface. Except from this area, most of the south polar layered deposits are covered by dust. Some parts of the north polar layered deposits are covered by dust as well [3].



Figure 1: The north permanent polar cap as it appears during the summer period. The white surfaces are the H₂O ice that is exposed during the summer season. (NASA/JPL/Malin Space Science Systems)

Airborne dust particles in the Martian atmosphere are deposited on the polar layered deposits and affect the interactions between the atmosphere and the H₂O ice. On top of the ice, a layer of dust or dust mixed with ice, influences the exchange of water vapor with the atmosphere by several processes: Water vapor diffuses through the dust layer and the layer changes the albedo and the conductivity of the top layer.

Studies of terrestrial glacier responses to tephra deposition (volcanic ash particles) show that the relationship between the thickness of the tephra cover and the ablation rates are not simple [5]. Small thicknesses lead to an increase in the ablation, while thicknesses larger than a critical value lead to a decrease in the ablation of the glacier. Clearly, these effects are due to the balance between increased absorption of shortwave radiation because of lower albedo and decreased conductivity in the upper layer of the glacier because of the tephra [5].

In this study, we will investigate the effects of an upper layer of dust mixed with ice on the sublimation rates of H₂O from the polar layered deposits, by modeling the water vapor transport through this layer.



Figure 2: The south permanent polar cap as it appears during the summer period. The white surfaces are the residual CO₂ ice that remains during the summer season. (NASA/JPL/Malin Space Science Systems)

Approach: We use a model inspired by a model developed by Schorghofer and Aharonson [6]. Their model simulates the ice deposition in the upper part of the subsurface on Mars by modeling the water vapor transport. The vapor undergoes phase transitions to free ice and/or adsorbed H₂O when the temperature changes throughout the Martian year. We modify this

model to calculate how the water vapor sublimation from the ice cap is affected by a top dusty layer.

Thermal conduction in the dusty layer and water vapor diffusion through the layer are both simulated with a one-dimensional model. The thermal part is solved with a Crank-Nicholson scheme, which is unconditionally stable and allows us to resolve both diurnal and seasonal time scales. The upper boundary condition consists of the surface temperature obtained from the energy balance for the surface. As the lower boundary condition, we apply a geothermal heat flux of 0.028 Wm^{-2} . In the diffusion part, we have a set of equations expressing the change in ice content and partial pressure of H_2O as a function of time. These equations are solved explicitly. As upper boundary conditions, we use the water vapor content obtained with TES-data [7] and assume a permeable surface. The lower boundary condition consists of the vapor flux from the ice cap.

This model should be able to resolve the sublimation problem on shorter as well as longer time scales.

Discussion: We will determine sublimation rates of H_2O from the polar layered deposits as a function of the thickness of a surface layer of dust. We will report the results from the modeling and their implications to the understanding of the interaction between H_2O in the polar layered deposits and the atmosphere.

In addition, our results may also be useful for interpreting the data from the coming Phoenix mission to the north polar region of Mars [8].

References: [1] Smith, M. D. (2002) *J. Geophys. Res.*, 107(E11), 5115. [2] Titus T.N. Kieffer H.H. and Christensen P.R. (2003), *Science*, 299, 1048 – 1051. [3] Clifford S.M. et al (2000), *Icarus*, 144, 210-242. [4] Smith, D.E., Zuber, M.T. and Neumann G.A. (2001) *Science*, 294, 2141-2146. [5] Kirkbride M.P. and Dugmore A.J. (2003) *Journal of Glaciology*, 49, 420-428. [6] Schorghofer, N. and Aharonson O. (2005) *J. Geophys. Res.*, 110, E05003. [7] Smith, M.D., (2006) *Second workshop on Mars atmospheric modeling and observations. Granada, Spain, 2006*. [8] <http://phoenix.lpl.arizona.edu/>

Acknowledgements: We would like to thank Norbert Schorghofer for helpful comments to the modeling and Michael D. Smith for sharing the TES-data in electronic form with us.

Quantitative Comparison Between Burial Depths of Hydrogen Inferred from Neutron Data and Ground-Ice Stability Models. W.C. Feldman¹, M.T. Mellon², O. Gasnault³, B. Diez³, R.C. Elphic¹, J.J. Hagerty¹, D.J. Lawrence¹, S. Maurice³, T.H. Prettyman¹, ¹Los Alamos National Laboratory, Los Alamos, NM, USA (wfeldman@lanl.gov), ²Laboratory for Atmospheric and Space Physics, Colorado University, Boulder, Co, USA, ³Centre d'Etude Spatiale des Rayonnements, Toulouse, Fr.

Introduction: Many theoretical studies starting with Leighton and Murray (1966) [1], predict that ground ice should be stable at ever shallower depths as latitude increases at high latitudes on Mars. The existence of such deposits has been inferred from neutron leakage currents measured using the GRNS suite of instruments aboard Mars Odyssey [2]. The boundary between enhanced hydrogen abundances at high latitudes and moderate abundances at mid to low latitudes is quite sharp [3], in agreement with these models [e.g., 4,5]. However, all models require a host of assumptions to obtain quantitative predictions of ice burial depths. These include estimates of the water-vapor density, near-surface rock density, abundance and types of hydrous minerals, permeability of surface soils, albedo, slope, thermal inertia, and mean annual surface temperature. Similar (but different) problems affect interpretations of measured neutron data to infer burial depths. For example, thermal neutron leakage currents reflect both the elemental composition of surface soils and the stratigraphy of its hydrogen content in non-separable combinations. The Mars Odyssey Neutron Spectrometer (MONS) only measures three neutron energy bands, which therefore requires a simple model that contains three or fewer free parameters. The model used here has a two-layered stratigraphy that consists of a horizontally infinite upper layer that contains W_{up} mass fraction of water-equivalent hydrogen having a depth, D (in units of g/cm^2), and overlying a semi-infinite layer of soil that contains W_{dn} of hydrogen. The elemental composition of

both the top and bottom layers needs to be specified *a priori*. All these assumptions are so central to determining the distribution of water-equivalent hydrogen that it is important to quantitatively compare the predictions of these models with the depths inferred from neutron measurements.

Methodology: The model adopted for our study was developed by Mellon and coworkers [7,8]. It was smoothed using a 240 km FWHM Gaussian filter and rebinned onto a $2^\circ \times 2^\circ$ cylindrical equal-angle mapping grid. Predicted ice-table depths were converted to g/cm^2 by multiplying depths in cm by an assumed density of $1.65 g/cm^3$. The three energy bands measured by MONS (thermal, epithermal, and fast neutrons) were also binned on a $2^\circ \times 2^\circ$ mapping grid after similar smoothing. The measured thermal and epithermal neutron currents were then converted to a W_{dn} mass fraction and D using a grid of currents simulated using MCNPX [2] for a composition that has a macroscopic absorption cross section identical to the average of compositions measured at the Viking and Pathfinder landing sites. These soils should be representative of those that blanket the high northern latitudes between 45° and 75° N. This region appears to be relatively young and covered by a thick veneer of wind-blown dust that originated in the outflow channels near all three of these landing sites (e.g., [6] and references therein). A similar procedure was used to place limits on W_{up} using the measured fast and epithermal neutron currents.

Results: Examples of the derivation of the burial depths, D , from measured

thermal/epithermal and fast/epithermal neutron counting rate correlations and their simulated rates using MCNPX, were given previously [7]. The fast/epithermal correlations for measurements between 60° and 75° N favor a W_{up} between 1% and 5% but rule out 10%. These results are generally consistent with W_{up} estimated from OMEGA data [8]. An overview of both model depths and depths inferred from thermal and epithermal neutron data is shown in the left-hand panel of Fig. 1. The two generally agree for atmospheric water vapor contents between 10 precipitable microns (10 prm) and 20 prm, but disagree strongly at about -110° E longitude and between about -30° E and $+80^\circ$ E. We do not yet understand the cause of this disagreement. Both model and neutron data show that burial depths generally increase with decreasing latitudes in the latitudinal band where the model predicts burial depths to be less than 1 m, as shown at the right in Fig. 1. This result does not hold near -110° E and between -30° and $+80^\circ$ E. It also does not hold at the highest latitudes between $+137^\circ$ and $+180^\circ$ E because of the presence of outlier surface ice that is not accounted

for by the model. However, whereas the model depths increase sharply between about 55° and 65° N (not shown because they rise so steeply), the neutron burial depths peak between about 55° and 60° N. The latitude width of this peak is generally narrow compared with the MONS spatial response function so that the real peak could be very sharp, in better agreement with the model, but occurs at a slightly lower latitude. This peak most likely marks the spatial boundary between mixed water ice and hydrated mineral deposits north of about 60° N, and primarily hydrated mineral deposits south of 60° N [7].

References[1] Leighton, R.G., B.C. Murray, *Science*, 153, 136-144, 1966, [2] Prettyman, T.H., et al., *JGR*, 109, E05001, doi:10.1029/2003JE002139, 2004, [3] Tokar, R.L., et al., *GRL*, 29, 1904, doi:10.1029/2002GL015691, 2002, [4] Mellon, M.T., B.M. Jakosky, *JGR*, 98, 3345-3364, 1993, [5] Mellon, M.T., et al., *Icarus*, 169, 324-340, 2004, [6] Tanaka, K.L, *JGR* 108, doi:1029/2002JE001908, [7] Feldman, W.C. et al., *LPSC XXXVII*, Abs. 2246, 2006, [8] Milliken, R.E., et al., *LPSC XXXVII*, Abs. 1987, 2006.

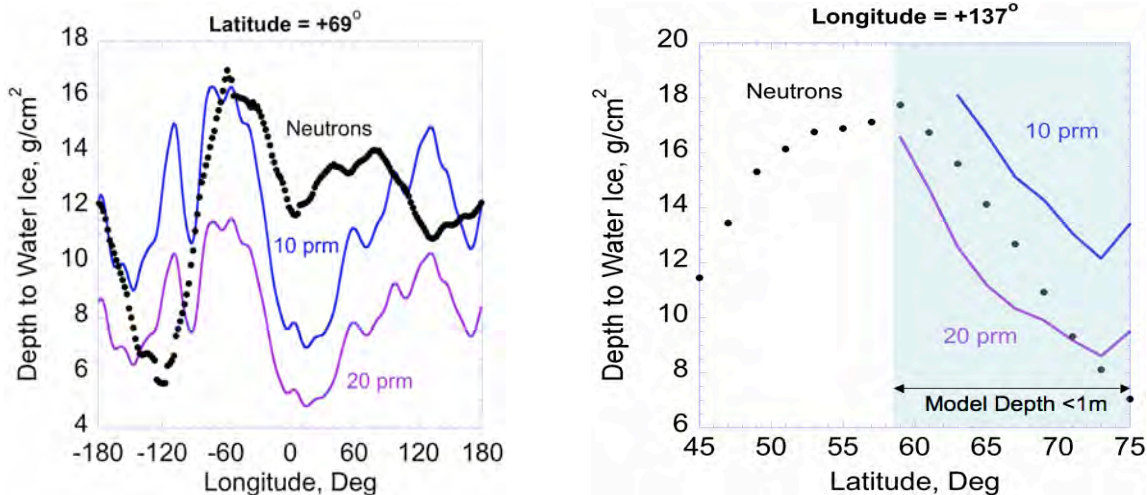


Figure 1. Burial depths to the ice table predicted by the model (blue and purple) and inferred from measured neutron data for all longitudes at $+69^\circ$ latitude (left) and for latitudes between 45° and 75° N at $+137^\circ$ E longitude.

STRATIGRAPHY AND ACCUMULATION RATES OF THE NORTH POLAR LAYERED DEPOSITS WITH IMPLICATIONS FOR FLOW K. E. Fishbaugh¹ and C. S. Hvidberg², ¹International Space Science Institute, Hallerstrasse 6, Bern CH-3012 Switzerland, fishbaugh@issi.unibe.ch, ²Niels Bohr Institute, University of Copenhagen, Juliane Maries Vej 30, Copenhagen DK-2100, Denmark, ch@gfy.ku.dk.

Introduction: To unravel the complex climatic record within the polar layered deposits (PLD), a better understanding of their geologic history is necessary. As one step in discovering this history, one must know the stratigraphic relationships and accumulation rates within the PLD.

Several authors have investigated the stratigraphy of the polar layered deposits within local troughs [e.g., 1, 2, 3] and across several troughs [e.g., 4]. Two recent studies have determined that the internal layer structure of both PLD may be curving downwards, away from the PLD center [5, for the southern PLD; and 6, for the northern PLD].

In this study [7], we correlate individual layers across the north PLD using MOC images and MOLA data, thus obtaining PLD-wide stratigraphic information. Additionally, we can derive the relative net mass balance for entire layer sequences at various points using our layer correlations. From these correlations, we can also assess whether flow has significantly affected the layer structure. Thus this study adds important insight into the depositional and flow history of the north PLD.

Correlating Layer Sequences: We have performed our layer correlations using MOC images of the PLD exposed in trough walls and MOLA data which provide the elevation of each correlated layer. Figure 1 shows a map of the images used for correlations. We have identified an Upper Layer Sequence (ULS) and a Lower Layer Sequence (LLS) stratigraphically below the ULS. The layer correlations are not based on being able to identify individual layers from one image to the next but rather on being able to match the sequence of individual reference layers. This method is explained in more detail in [7].

Derived Stratigraphy: The layer structure derived from our correlations is shown in Fig. 2. Layer dips along troughs are similar to the PLD surface slope. Ignoring variation between them, the ULS and LLS slope downwards between the images closest to the pole and those at lower latitudes. On a vertical scale, however, height variations are significant compared to the ~3000 m combined thickness of the PLD and Basal Unit [8,9,10]. Since localized variations in layer height are not parallel between the ULS and LLS, these sequences have not been deposited conformably with each other. Mass

balance patterns must therefore have changed between the two units.

Relative Accumulation Rates: From our layer correlations across the PLD, we derive relative accumulation rates for the entire ULS and LLS, rather than for individual layers. As a first-order estimate, we can equate relative accumulation rate to the elevation difference between two specified layers in the ULS and two in the LLS without tying this to a timescale (Fig. 3). The relative accumulation rates for the ULS and LLS are calculated using different sets of layers, so one cannot directly compare the absolute values for the ULS and LLS but rather the overall trends.

From Fig. 3, it is evident that the accumulation rates of the ULS vary significantly, up to ~200%. We have no data for the ULS at latitudes lower than 86°, but there appear to be no overall trends in accumulation rate at these high latitudes, either with respect to latitude or longitude (not shown in Fig. 3). We cannot determine with these data whether the accumulation rate decreases at lower latitudes, towards the margin.

The LLS exhibit a larger variation in accumulation rate (up to ~300%), but that variability is almost completely within the error bars. The lesser thickness of the LLS as compared to the ULS results in larger errors in calculated relative accumulation rate. With respect to latitude, accumulation rates decrease away from the pole, unlike for the younger layers above (the ULS), but like terrestrial ice sheets. The LLS data cover a smaller range of longitudes than do the ULS data, but within this range, no trend is evident.

Of course, the absolute maximum and minimum relative accumulation rates for the ULS and LLS may occur at locations not represented by the data points shown in Fig. 3.

The differing patterns in at least the local variations in relative accumulation rate of the LLS and ULS indicate that the cap may not have ever been in a steady state. Additionally, accumulation rates and mass balance patterns have not remained constant through time nor are they spatially uniform.

Implications for Flow: We can also compare the derived stratigraphy with model predictions of the effects of large-scale flow on layer structure. We assume a northern PLD mass balance pattern and history, and use an ice flow model to simulate the

evolution until present. We simulate layers within the PLD by keeping track of past PLD surfaces at specific time intervals as they are buried and gradually begin to be affected by flow. The details of this model can be found in [7].

In Fig. 4 we show our results for a model run with an oscillating mass balance pattern and decreased accumulation rates near the margin (though never < 0). Here, we specify deposition of the PLD to begin 5 Mya and then allow them to evolve under deposition and flow. According to our model results, even the signature of an oscillating deposition may be almost completely erased by flow.

Our data show that the heights of the ULS and LLS layers are not smoothly varying. Thus, the ULS and LLS do not exhibit evidence of having been significantly affected by large-scale flow under the conditions modeled for this study. Flow rates have been slow compared to mass balance rates. However, it should be emphasized that the effects of flow on layers can be less pronounced at shallower depths (like those of the ULS and LLS) than at deeper depths, where flow may have acted for a longer time.

References: [1] Howard et al., *Icarus* 50, 161, 1982. [2] L. Fenton & K. Herkenhoff, *Icarus* 147, 433, 2000. [3] Malin, M. & K. Edgett, *JGR* 106 (E10), 23,429, 2001. [4] E. Kolb & K. Tanaka, *Icarus* 154, 22, 2001. [5] S. Byrne & A. Ivanov, *JGR* 109 (E11), 2004. [6] S. Milkovich & J. Head, *JGR* 110 (E05), 2005. [7] K. Fishbaugh & C. Hvidberg, *JGR*, 10.1029/2005JE002571, 2006. [8] S. Byrne and B. Murray, *JGR* 107 (E6), 2002. [9] K. Edgett et al., *Geomorph.* 52, 289, 2003. [10] K. Fishbaugh & J. Head, *Icarus* 174, 444, 2005.

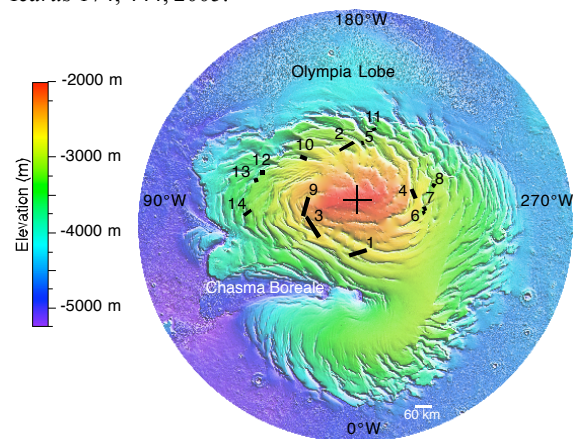


Fig. 1. Map showing locations of images used for correlation in this study. Cross in the center indicates location of the pole. Map is 960 km across. Marks show image location and orientation but not image size. Base map is the MOLA 512pix/degree gridded MOLA topography. Images are numbered as in Figs. 2 & 3.

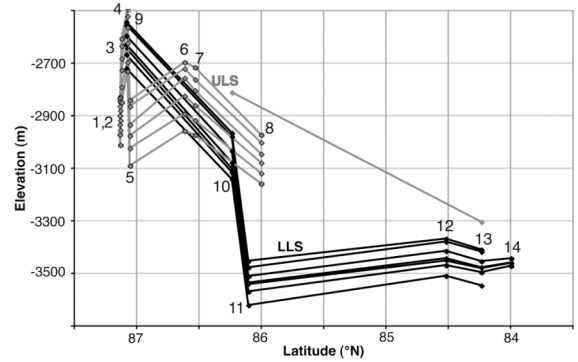


Fig. 2. Elevation of the ULS (grey) and LLS (black) as a function of latitude (°N). We estimate a maximum vertical positioning error of about ±5 m. Each vertical stack of points comprises an exposure of the ULS or LLS in one MOC image. Note that this figure does not represent a true cross-section.

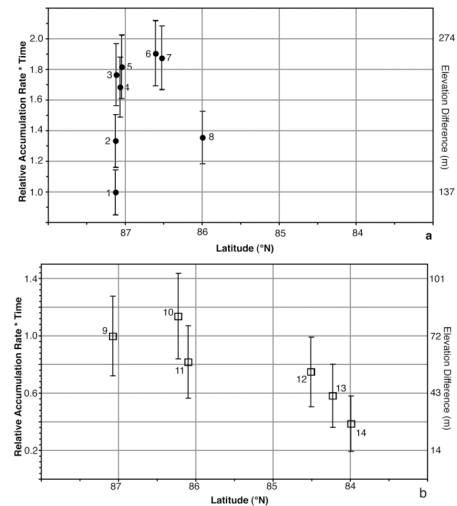


Fig. 3. Relative accumulation rates for (a) the ULS and for (b) the LLS. The relative accumulation rate values have been normalized to those of the images closest to the pole.

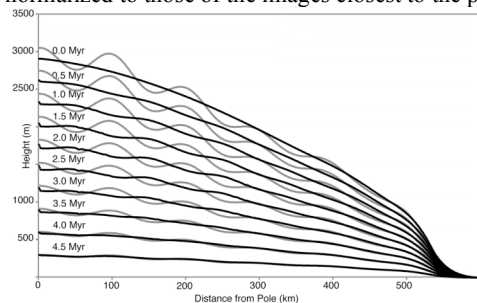


Figure 4. Flow model run illustrating the effects of flow on large-scale layer structure after 5 Myr of evolution. Black lines are the layers after flow, and grey lines are the layers with no flow (only accumulation). Simulated internal layers (i.e. former PLD surfaces) are labeled by their age. The PLD builds up with the varying mass balance pattern but is allowed to flow as it builds up. Flow smooths the mass balance pattern.

FORMATION OF THE MARTIAN NORTH POLAR GYPSUM DEPOSIT DURING THE AMAZONIAN

K. E. Fishbaugh¹, F. Poulet², Y. Langevin², V. Chevrier³, and J-P. Bibring². ¹International Space Science Institute (ISSI), Hallerstrasse 6, Bern CH-3012 Switzerland, fishbaugh@issl.unibe.ch. ²Institut d'Astrophysique Spatiale (IAS), Bâtiment 121, 91405 Orsay Campus, France. ³CEREGE, Europôle de l'Arbois, BP80, 13545 Aix-en-Provence Cedex 04, France.

Introduction: Based on global mineralogical mapping by OMEGA, *Bibring et al.* [1] have created an alternative timescale for Mars based on mapping of minor mineral phases with significant geological implications. The Theikian (Early to Mid Hesperian) is characterized by alteration of clays and mafics into sulfates and deposition of sulfates as evaporites. The dry surface of Mars that we see today is hypothesized to have existed throughout the Siderikian (Late Hesperian to Amazonian), with short-lived interruptions (e.g., outflow channels). However, OMEGA also detected the largest gypsum (Ca-sulfate) deposit on Mars within the Amazonian-aged dunes in the north polar region [2], apparently confounding this alternative timeline system. Here, we discuss the origin of this gypsum in an environment unique to the north polar region and how its presence does not contradict the hypothesized global patterns of mineralogy through time.

Gypsum on Earth and Mars: Gypsum is a hydrated Ca-sulfate ($2\text{H}_2\text{O}\cdot\text{CaSO}_4$). Gypsum can be formed, for example, as a hydrothermal deposit [3], as an alteration product of iron sulfide [4] or Ca-bearing, mafic minerals, or as an evaporite in acidic water. Gypsum is soft and thus easily susceptible to physical weathering and is light in color.

On Mars, in addition to the north polar deposit, the OMEGA team has tentatively identified gypsum as one constituent in the layered deposits of Juventae Chasma [5]. The MER Opportunity rover has also detected small amounts of Ca-sulfate salts at Meridiani Planum [6] which may have been created by evaporation of fluids involved with weathering of basalts [7].

Observations in the North Polar Region: *Langevin et al.* [2, 8] have identified gypsum in the north polar region mainly by the strong 1.94 μm absorption feature in OMEGA spectra of the sand sea. In Fig. 1, we map the 1.94 μm feature using the 1.927 μm OMEGA channel in order to reduce contamination by atmospheric CO_2 ; it is essentially a map of gypsum concentration (purple: 6% band strength; red: 40%). We are currently investigating the translation of band strength into weight or volume percent, but we estimate that the highest concentrations are about 60 weight%. For the most part, the dunes consist of pyroxene, with the concentrations of pyroxene and gypsum having an

approximately inverse relationship. We find that gypsum exists only in the presence of dunes. In other words, OMEGA does not detect gypsum anywhere where dunes are not present.

We have further investigated this relationship with the dunes by examining MOC images; we find that there is no correlation of gypsum concentration with dune morphology. Additionally, there are no obvious albedo anomalies associated with the gypsum so that it is not forming surficial crusts or windblown, fine-particle, surface deposits. No apparent color anomalies manifest themselves either in THEMIS or HRSC color images. THEMIS IR data indicate that no temperature anomalies exist in the gypsum area, implying that these dunes may have a similar thermal inertia to the gypsum-poor dunes.

These observations suggest that the gypsum is intimately mixed with the saltating sand. The low albedo (16% at 1.2 μm [8]) of even the dunes containing gypsum indicates that the gypsum grains probably contain dark, mafic inclusions. There are several reasons why gypsum would be associated with sand dunes. 1) The formation of dunes requires sand-sized particles so that within the dunes, all other species having different particle sizes have been removed, helping to concentrate the sand-sized gypsum here. 2) In areas without dunes or other sediments, gypsum (and any other wind-blown sediment) is being distributed by the wind rather than deposited. 3) At the wavelengths used to detect gypsum, OMEGA is most sensitive to sand-grained size particles. Minor amounts of undetectable finer-grained gypsum may exist elsewhere. 4) As discussed below, formation of gypsum would most likely occur where Ca-bearing minerals (in the dunes) are present.

Origin of the Gypsum: *Byrne and Murray* [9] and *Fishbaugh and Head* [10] have identified the north polar Basal Unit, lying stratigraphically beneath the polar layered deposits, as the main, if not sole, source for the north polar sand sea. However, high resolution OMEGA data (at 1 km pixel) reveal a gap between areas containing high gypsum concentration and the polar layered deposits (Fig. 2). This gap is occupied by the Basal Unit. Thus, it appears that the Basal Unit is not the source for the gypsum within the dunes.

Since gypsum is a soft mineral, it cannot saltate long distances. Thus, one would expect the gypsum source region to lie close to or within the highest gypsum concentrations. As shown in the map in Fig. 1, sinuous valleys extending from the polar layered deposits terminate just to the east of the high-gypsum area. We hypothesize that the most likely origin of these valleys is fluvial erosion resulting from the melting and outflow event which initiated the formation of Chasma Boreale to the east [11]. An alternate or additional water source could be the formation of the nearby impact crater which may also have caused the polar layered deposits in this region to melt. Note that small amounts of gypsum (associated with dunes) surround the region where the channels terminate. Currently, younger, higher albedo material (likely frost and dust) covers this area, masking any putative gypsum signature within it. Sulfur could exist in abundance in the soil from earlier volcanism and even from putative nearby volcanoes identified by the HRSC team [2/25/05 press release image, ESA website], and calcium may exist within the pyroxene of the dunes. Having identified the sources of chemistry and water to produce the gypsum, the question now becomes, "Did the gypsum form as a true evaporite or as a weathering product?"

For the gypsum to have formed as a true evaporite in a basin, a complex chain of events must have occurred. Alteration of the pyx-bearing dunes themselves proves a much simpler scenario; note that this is contrary to what we have previously asserted [12]. In this case, the acidic water circulated within the dunes, which were easily altered because of the large surface area exposed (due to the many grains). This alteration has then removed much of the pyroxene in that area. If the deposits near the mouths of the channels have been altered at all, there is no evidence in the OMEGA data, perhaps due to the fact that younger materials (likely mostly ice and dust) cover these deposits.

Conclusions. We propose that the north polar gypsum deposit was formed due to in-situ alteration of pyx-bearing sand dunes by S-rich water emanating from the Chasma Boreale melting event and/or from melting due to the nearby impact into ice. Thus, this melting event and the presence of many easily altered, pyx-bearing dunes near the mouths of meltwater channels conspired to create a unique situation wherein gypsum was able to form, even within the Siderikian (Amazonian).

Future work will include better estimates of the total amount of gypsum, investigation into whether other, secondary alteration products exist in this area,

and more thorough characterization of dune composition. We also plan to fully characterize the geologic and geochemical sequence of events in creating this gypsum deposit.

References: [1] J.-P. Bibring, et al. (2006), *Science*, 312, 400-404. [2] Y. Langevin, et al. (2005), *LPSC*, 36, Abs. 1652. [3] J. Martinez-Frías, et al. (2004), *Earth, Planets and Space*, 56, v-viii. [4] R. Burns, et al. (1990), *JGR*, 95, 14,415–14,421. [5] A. Gendrin, et al. (2005), *Science*, 307, 1587-1591. [6] S. Squyres, et al. (2004), *Science*, 306, 1709-1714. 10.1126/science.1104559. [7] N. Tosca, et al. (2005), *Eos Trans. AGU*, 86, Abstract P12A-07. [8] Y. Langevin, et al. (2005), *Science*, 307, 1584-1586. [9] S. Byrne, et al. (2002), *JGR*, 107, 10.1029/2001JE001615. [10] K. Fishbaugh, et al. (2005), *Icarus*, 174, 444-474. [11] K. Fishbaugh & J. Head (2002), *JGR*, 107, 10.1029/2000JE001351. [12] K. Fishbaugh, et al. (2006), *LPSC*, 37, Abs. 1642. [13] H. Tsoar et al., *JGR* 82, 8167, 1979.

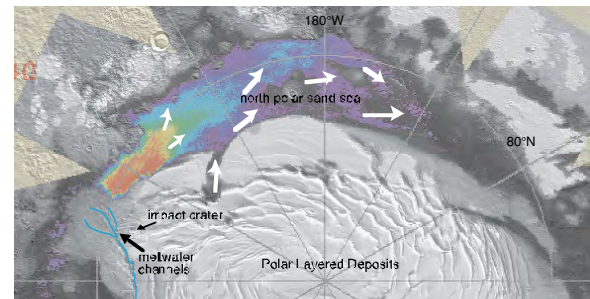


Figure 1. Map of gypsum band strength in the north polar region. Modified from [8]. Arrows indicate wind direction as mapped by Tsoar et al. [13] from dune morphology.

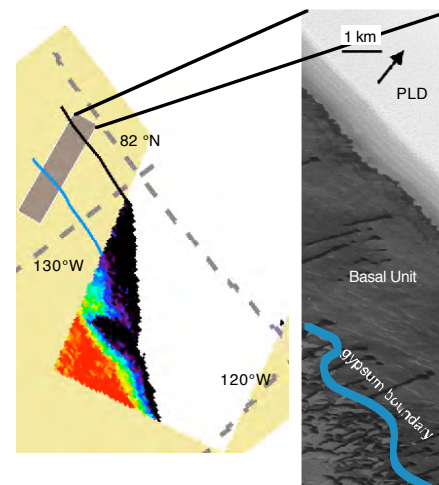


Figure 2. Illustration of the lack of gypsum in the polar Basal Unit. *Left:* High resolution OMEGA data (1 km/pix) showing gap between the gypsum-rich dunes and the polar layered deposits. *Right:* MOC image showing presence of layered Basal Unit occupying that gap. Arrow indicates sun direction.

Sensitivity of D/H in Mars Atmosphere to Time Varying Processes in the Water Cycle, Water Reservoir Sizes and Exchange Rates ; What D/H History Might Be Found by Drilling in The North Polar Cap and What it Might Mean.

David Andrew Fisher

Glaciology Section , Geological Survey of Canada. NRCan , 601 Booth Street ,Ottawa Ontario K1A 0E8,Canada, david.fisher@nrcan.gc.ca

Introduction

A time varying stable isotope model for the D/H history of Mars water cycle is developed with variable atmosphere, space loss rate , ground and ice cap flux rates. It considers coupled ground reservoirs and traces D/H in the air and reservoirs secularly and over obliquity cycles. The various flux rates are prescribed time variables that simulate changes due to constant losses and cyclic obliquity and solar driven space loss rates. Predicted bulk averages for the ice cap , ground ice reservoirs and atmosphere span the observed ranges reported by Mumma et al. (2). The more likely obliquity cycle variations scaled so that the model delivers present seasonal variations suggests the present long term bulk D/H average for the ice cap is $\sim +2.7$ (equivalent to $+1700$ o/oo in (D) wrt SMOW) . The obliquity driven D/H cycle in the ice caps layer varies between 3 and 6. The smaller more accessible reservoirs have larger bulk averages with the smallest being able to reach D/H values over 9 within $\sim 10^5$ years. Small hypothetical solar activity driven variations in the escape rate to space and in the fractionation constant (Krasnopolsky and Feldman ,1) for the escape process can produce a “solar wiggle” whose D/H amplitude can reach 0.1 ((D) amplitude of 100 o/oo). Because of the temporal variability of D/H ,a single modern measured D/H ratio at a particular Ls can not tell very much about the total water inventory of Mars. A bulk average for the Northern Ice Cap and better still a dated vertical profile of D/H from the ice cap would , however, go a long way towards illuminating the “modern” water history of Mars . The age and stability of the Northern Ice Cap and the D/H history locked in the layering is discussed . An ice cap that is very young and exchanges its mass through the atmosphere often will necessarily have a large D/H .

References:

- 1)Krasnopolsky V.A. and Feldman P.D. 2001.*Science*, **294**, 1914-1917.
- 2)Mumma M.J., et.al. . 2003. Seasonal mapping of HDO and H₂O in the Martian atmosphere. Conference Reports of “Sixth International Conference on Mars Atmosphere” No.3186.

ICE CAPS, GLACIERS AND GULLIES: THE EFFECT OF OBLIQUITY ON MARTIAN CLIMATE. F. Forget¹, F. Montmessin², B. Levrard³, R.M. Haberle⁴, J. W. Head⁵, J.-B. Madeleine^{5,1} ¹Laboratoire de Météorologie Dynamique, IPSL, Université Paris 6 BP99, 75005 Paris (forget@lmd.jussieu.fr), ². Service d'Aéronomie, CNRS, Verrière le Buisson, France ³IMCCE, Obs. de Paris, France ⁴NASA Ames Research Center ⁵Brown University, Providence, USA

Introduction Surface conditions on Mars are currently cold and dry, with water ice unstable on the surface except near the poles and surface liquid water thought to be never present. However, geologically recent glacier-like landforms have been identified in the tropics and mid-latitudes of Mars, an ice-rich mantling seems to cover both hemisphere above 60° latitude, and recent gullies apparently carved by liquid-water rich debris flows are observed. The corresponding climate changes seem to have been recorded in the multi-layered polar deposits.

Modelling the water cycle in the past. To better understand the climate conditions and processes that have formed such features, we have conducted a first set of studies by adapting models used to simulate present-day Mars to other orbital and obliquity parameters.

First, we have performed high resolution climate simulations with a numerical model designed to simulate Mars current climate [1] and the details of the present-day Mars water cycle [2], but using different obliquities, like on Mars a few millions of years ago.

At high obliquity (e.g. 45°), the model predicts the accumulation of ice and the formation of glaciers on the western flanks of the great Tharsis volcanoes if the current northern polar cap remains a source of water, and in eastern Hellas if a water ice polar cap is assumed to be present at the southern pole [3] This is precisely where the most characteristic Glacier-like features have been discovered. The agreement between observed glacier landform locations and model predictions points to an atmospheric origin for the ice and permits a better understanding of the details of the formation of Martian glaciers.

Using the same model, we show that when Mars returns to lower obliquity conditions, the low and mid-latitude glaciers becomes unstable, partially sublimates and tend to accumulate in both hemisphere above 60°. Once water is no more available from the low and mid-latitude glaciers, water tends to return to the poles (where it is now), but probably leave some ice under a dry layer. We suggest that such a processes probably explain the presence of the ice-rich mantling observed by geomorphology and detected by the GRS instrument aboard Mars Express [4]

In this scenario, the formation of glaciers and ice layers on Mars is the product of the same Martian climate system as that of today, except that the enhanced water cycle allows the precipitation and accumulation of ice in specific locations controlled by the atmospheric circulation. In reality, the complex variations of orbital parameters probably led to all sorts of regimes in the past, with water ice alternatively mobilized from the poles to the tropical and mid-latitude glaciers and to the high latitudes. In Davos, new results obtained with new combinations of orbital parameters leading to accumulations of ice in new regions will be presented.

After several obliquity cycle, all these processes should have created layers that could be detected by Phoenix in 2008. Moreover, on the basis of the ice accumulation or loss rate that are modeled at the pole, we can try to reconstruct the history of the ice accumulation at the North pole in the past 10 Million years and compare the modeled layers with the actual structures that are observed in the polar deposits throughs [5].

It is also likely that some of the past Mars Climate regimes led to the accumulation of ice on slopes that could have had reached the melting point of water and initiate debris flows and Gullies, in some specific conditions that we can investigate with the climate models [6].

Overall, we can thus propose a simple, consistent scenario to explain the formation many of the amazonian icy landforms by the climate system that we know today, without the involvement of subsurface reservoir.

Some Issues

Large uncertainties that remains in the current past climate simulations and that could be addressed by the Mars atmosphere community. For instance, the radiative feedback of water ice clouds and water vapor may play a role, but we do not yet take them into account. Another uncertainty is atmospheric dust, which has a strong impact on our results. In particular, the amount of dust present in the atmosphere at high obliquity is unknown. GCM simulations show that the near-surface circulation amplifies considerably with increasing obliquity [7,8] such that potential dust lifting could be much higher than today. However, the

atmospheric dust load may have been limited by the finite amount of surface dust available in the windy locations so that the opacity may not have been higher than today. In any case; in the ice accumulation region, precipitations should have contributed to the cleaning of the atmosphere by scavenging dust particles, as on Earth today. Such a process should be investigated in future studies. Similarly, the formation of lag deposits on sublimating water ice reservoir remains to be well understood, as well as the local stability of water ice and liquid water.

Our current simulations are not yet able to predict and explain all the ice-related deposits that are observed on Mars. The most striking example is the Deuteronilus-Protonilus Mensae region (0-80°E, 30-50°N), where large concentrations of lobate debris aprons and lineated valley fills (that resemble flow lines in glacial ice on Earth) are found. We do not predict glacier formation there and in other similar areas in the northern mid-latitudes. These accumulations might have involved climate changes due to other origins (impacts, volcanism, catastrophic outflows). However, on the basis of some recent simulations performed with high dust loading, we are more and more convinced that some combination of orbital parameters or a higher model resolution may be sufficient to simulate ice precipitation in this region without invoking other processes.

Reference

- [1] Forget, F., F. Hourdin, R. Fournier, C. Hourdin, O. Talagrand, M. Collins, S. R. Lewis, P. L. Read, and J-P. Huot. An improved general circulation model of the Martian atmosphere from the surface to above 80 km. *J. Geo. Res.* 104, 24,155-24,176, 1999.
- [2] Montmessin, F., F. Forget, P. Rannou, M. Cabane and R. M. Haberle The origin and role of water ice clouds in the Martian water cycle as inferred from a General Circulation Model *J. Geophys. Res.* 109, E10, CiteID E10004 (2004)
- [3] Forget, F.; Haberle, R. M.; Montmessin, F.; Levrard, B.; Head, J. W. Formation of Glaciers on Mars by Atmospheric Precipitation at High Obliquity *Science*, 311 pp. 368-371 (2006).
- [4] B. Levrard, F. Forget, F. Montmessin, and J. Laskar. Formation of recent martian high-latitude ice-rich deposits by sublimation of unstable equatorial ice at low obliquity . *Nature*, 431, 2004.
- [5] B. Levrard, F. Forget, F. Montmessin, and J. Laskar. A GCM recent history of martian layered deposits. submitted to *Jour. Geophys. Res.*
- [6] F. Costard, F. Forget, N. Mangold, and J. P. Peulvast. Formation of Recent Martian Debris Flows by Melting of Near-Surface Ground Ice at High Obliquity. *Science*, 295:110-113, 2002.
- [7] R. M. Haberle, J. R. Murphy, and J. Schaeffer. Orbital change experiments with a Mars general circulation model. *Icarus*, 161:66–89, January 2003.
- [8] C. E. Newman, S. R. Lewis, and P. L. Read. The atmospheric circulation and dust activity in different orbital epochs on Mars. *Icarus*, 174:135–160, 2005.

UNCONFORMITY AND BEDDING ORIENTATIONS IN PLANUM BOREUM, MARS: PRELIMINARY RESULTS AND DISCUSSION. C. M. Fortezzo^{1,2} and K. L. Tanaka², ¹Department of Geology, Northern Arizona University, Flagstaff, Arizona, cmf72@nau.edu, ²U.S. Geological Survey, Flagstaff, AZ 86001, ktanaka@usgs.gov.

Introduction: The polar layered deposits (PLDs) of Planum Boreum consist of upper layered deposits (ULDs) and lower layered deposits (LLDs) that are separated by an erosional surface expressed as an unconformity. We are measuring the orientations and mapping the locations of the ULDs, lower layered deposits LLDs and unconformity surfaces within the PLDs of Planum Boreum, Mars. Our goals are: (1) to better understand the relationship between unconformities and their adjacent layers and troughs in which they lie, and (2) to test existing formational mechanisms (e.g., [1-6]) and, if need be, to develop alternate formational mechanisms that help explain the evolution of the erosional and or non-depositional surfaces within the PLD.

Methods: We have mapped unconformities and beds in the PLD using ArcGIS on a basemap of 115 m/pixel resolution MOLA topography data overlain by hundreds of mosaicked ~19-17 m/pixel THEMIS VIS images and selected <10 m/pixel resolution THEMIS and where available, MOC narrow angle images. The mapped unconformities (Fig. 1) represent only a sample of the total number region the plateau as mapping is ongoing and correlate to unconformities previously identified in MOC narrow angle images [1]. We map one ULD bed above and one LLD bed below their corresponding unconformity.

The ArcView 3.2 three-point problem calculator extension determines the dip magnitudes and directions of unconformities and the associated ULD and LLD using elevation data from the 115-m/pixel

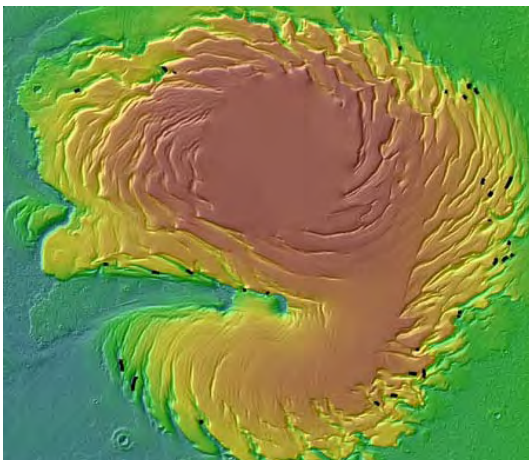


Fig. 1: MOLA-based color shaded relief map of Planum Boreum, Mars (warmer colors are higher elevations). The black lines are the mapped and measured unconformities.

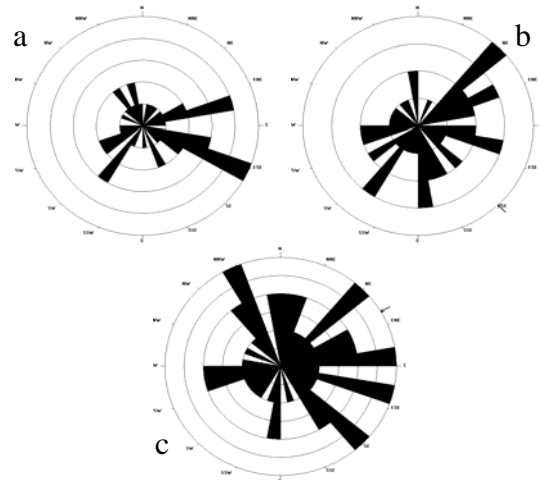


Fig. 2: Rose diagrams of the dip azimuths for the surfaces in this study. Data is separated into 36 10° bins and the great circle interval is 1 data point. (a) 53 measured PLD unconformity, note the east-southeast dominant orientation. (b) 49 LLD azimuths with a dominant dip-direction to the south-southeast. (c) Diagram of the 50 ULD azimuths indicating the trend of the data is to the east-northeast.

MOLA digital elevation model in a polar stereographic projection. We plot the orientation data in a rose diagram to resolve the dominant orientations (Fig. 2). These plots delineate dominant bedding orientations and provide a way to conveniently display trends in the data. However, the unconformity dip-directions and their relationship to their associated ULD and LLD bedding orientation are distinctive and further analysis is necessary to interpret individual sets and is discussed below.

Results: The map (Figure 1) shows 53 distinct unconformities distributed throughout Planum Boreum. The surface expressions of the unconformities are randomly orientated with respect to each other but the dip-direction is typically perpendicular to the troughs in which they lie.

Three-point solutions for the measured unconformities yielded a range of dip-directions (17° - 356.6°) and dips (0.1° - 83.9°). Measured bedding orientations below the PLD unconformities range from 0.3° - 353.8° for dip-direction and 0.3° - 25.3° for dip. The range of dip-direction for ULD is 0.3° - 351.5° and dip is 0.5° - 74.5°.

The rose diagrams representing unconformities, LLD and ULD (Figure 2a, 2b and 2c, respectively) show an array of orientations within the dataset. Significantly, we find that a dominant, eastward orientation, mean resultant direction for the unconformities being 101°. This trend could be due to the location of many of the

unconformities used in the analysis and will be further examined as more unconformities are measured. There is also a less dominant trend to the southwest.

The mean dip-direction for the ULD and LLD differ from each other and from the unconformities. The mean resultant direction for the LLD is 136° whereas the ULD mean resultant direction is 60°.

Errors within these measurements were not quantified, but we recognize errors may occur because (1) the curvilinear expression and limited extent of some layers and unconformities is not ideal for calculating three-point solutions, (2) an order of magnitude difference in resolution between the images and topography data may cause the inadvertent measurement of the wrong layer and (3) registration errors of images to the MOLA base may cause discrepancies in the resultant data if the pixels are not aligned correctly. We attempted to assess the degree of error by taking multiple measurements at different locations along the same unconformity to test whether or not the measurements were reproducible.

Discussion: One scenario of trough formation involves insolation-induced ablation of equator-facing scarps and redeposition on flats and pole-facing scarps in stepped and troughed topographies as troughs migrate poleward [REF]; unconformities resulting from this process are expected to dip parallel to scarp dip trends [2-3]. Measurements of Planum Boreum scarp dip directions demonstrate predominantly a SSW direction [2]; thus this process may account for the less dominant unconformity set of trends directed to the south and southwest. However, this process does not account for the dominant east-trending dips.

The troughs are also perpendicular to katabatic (downslope) winds across Planum Boreum that deflect westward across Planum Boreum, which are consistent with the SW orientation of Chasma Boreale and of dune migration of Hyperborae Undae within the chasma and the SW to W dune migration of Abalos and Olympia Undae on the margins of Planum Boreum. However, these winds are oblique to perpendicular to most trough scarp orientations, thus the troughs cannot be directly attributed to katabatic winds.

An additional observation is that Planum Boreum is marked by gentle undulations that align with trough orientations. These undulations may form as a consequence of preferential dust accumulation where perennial ice exists. If during particular climate episodes the ice is preserved year-round where insolation is relatively low and removed where the insolation is high, differential dust and ice accumulation may occur, ultimately leading to trough

formation where scarps develop of sufficient steepness [4]. If this is the dominant mechanism for trough formation, then troughs do not migrate poleward significantly but can enlarge both by deepening and by elongation at their ends, particularly in the pole-ward direction

An additional mechanism to account for the PLD unconformities is that winds crossing topographic saddles between troughs may cause local erosion (perhaps via cavitation) or non-deposition of PLD [1], which could result in unconformities that dip parallel to the troughs in either direction.

Our mapping of Planum Boreum unconformities indicates that most occur within the deeper troughs that dissect thicker sections of PLD near the margins of the planum. Also, the unconformities commonly occur low within the PLD. We suggest that the majority of east-dipping unconformities result from major episodes of trough deepening, burial, and exhumation. Most of the eastern to southeastern terminations of the troughs have since been removed by retreat of the margin of Planum Boreum, whereas the western to northwestern terminations are nearly all preserved. This can account for the predominant eastward dip trends of unconformity surfaces. While troughs have continued to develop in higher PLD strata, they apparently have not experienced burial and exhumation that has been preserved in the long-term stratigraphic record. However, most of the ULD appear to rest unconformably drape the LLD, particularly where exposed on pole-facing trough scarps [1] and at lower latitudes and elevations. The unconformable parts of these uppermost PLD may be deposited and removed cyclically in response to variations in solar insolation, perhaps in part due to rapid removal of a dust- and sand-rich basal layer [5]. Thus, the unconformities in the lower PLD may represent more profound climate variations that occurred during the early stages of PLD development. A large section of the PLD may coincide with an abrupt decrease in obliquity at ~5 million years ago [6]; lower PLD unconformities may represent earlier climate oscillations.

Future work: We will continue mapping the unconformities and measuring their surface orientations as well as those of the overlying and underlying bedding. Detailing the azimuths of the curvilinear troughs and undulations and comparing those to the dip directions will enable us to test whether the relationships support particular and perhaps multiple trough formational hypotheses as indicated thus far.

References: [1] Tanaka, K.L. (2005) *Nature* 437, 991. [2] Howard A.D. (1978) *Icarus* 34, 581-599. [3] Howard A.D. et al. (1982) *Icarus* 50, 161. [4] Cutts J.A. et al. (1979) *JGR* 84, 2975-2994. [5] Rodriguez J.A.P. et al. (2006) *LPSC XXXVI* (abst.) [6] Laskar J. et al. (2004) *Icarus* 170, 343-364.

SCENARIOS FOR THE FORMATION OF CHASMA BOREALIS, MARS

Ralf Greve, Institute of Low Temperature Science, Hokkaido University, Kita-19, Nishi-8, Kita-ku, Sapporo 060-0819, Japan. E-mail: greve@lowtem.hokudai.ac.jp.

Introduction. An intriguing feature of the Martian polar caps is the presence of large chasms and smaller scarps/troughs which have no counterpart in terrestrial ice sheets. In this study, the focus is on Chasma Borealis, which cuts about 500 km into the western part of the north-polar cap (NPC). A possible explanation for its origin is a temporary heat source under the ice due to a tectono-thermal event or a volcanic eruption (see the discussions by Refs. [1] and [2]). This possibility will be explored by assuming a locally increased geothermal heat flux in the region of Chasma Borealis for a limited period of time in the past, and simulating the dynamic/thermodynamic response of the ice cap with the model SICOPOLIS (SIMulation COde for POLy-thermal Ice Sheets). The questions to be investigated are (i) how much geothermal heat over which amount of time is required to form the chasm, (ii) how much water is discharged by a process of that kind (catastrophic flooding?), (iii) what are the local ice-flow velocities at the slopes of the chasm, and (iv) which processes can keep the chasm open after the end of the heating event.

Modelling approach. The ice-sheet model SICOPOLIS describes the material ice as a density-preserving, heat-conducting power-law fluid with thermo-mechanical coupling due to the strong temperature dependence of the ice viscosity, and computes three-dimensionally the temporal evolution of ice extent, thickness, temperature, water content and age as a response to external forcing. The latter is specified by (i) the mean annual air temperature above the ice (surface temperature), (ii) the surface mass balance (ice accumulation minus melting and evaporation), and (iii) the geothermal heat flux from below into the ice body.

Items (i) and (ii) constitute the climatic forcing and are provided by the Mars Atmosphere-Ice Coupler MAIC. The current version MAIC-1.5 [3] is driven directly by the orbital parameters obliquity, eccentricity and anomaly of vernal equinox [4]. Surface temperature is parameterized by the Local Insolation Temperature (LIT) scheme [5], which uses a daily and latitude dependent radiation balance and includes a treatment of the seasonal CO₂ cap. Surface mass balance is parameterized by an equilibrium-line approach in analogy to terrestrial glaciology [2,6], with the present-day accumulation rate (of the order of 0.1 mm/a) as the main free parameter. As for item (iii), the geothermal heat flux, a standard value of 35 mW/m² is chosen. The assumed thermal anomaly under Chasma

Borealis is described by an increased heat flux, q_{CB} , between 100 mW/m² and 10 W/m² for the entire chasm area. The basal heat flux is imposed 5 km below the ice base, and any basal meltwater is assumed to be drained instantaneously.

Further settings include an elastic-lithosphere-relaxing-asthenosphere (ELRA) isostasy model with a lithospheric flexural rigidity of 10²⁵ Nm and an asthenospheric time lag of 3 ka [7,8], Glen's flow law with stress exponent $n = 3$ and activation energy $Q = 60$ kJ/mol [9], a spatially and temporally constant dust content of 20%, a grid spacing of 20 km and a time-step of 1 ka. Other physical parameters are the same as in Ref. [6].

Reference simulation of the NPC. This simulation is driven by the orbital parameters provided by Ref. [4]. Owing to the high obliquities prior to 5 Ma BP and correspondingly high summer evaporation rates, an ice-free initial state at $t = 5$ Ma BP is assumed, the simulation is run until the present ($t = 0$), and the accumulation rate is chosen such that the simulated present-day maximum surface elevation matches the observed value of -1.95 km w.r.t. the reference geoid [10,11]. This tuning procedure yields a present-day accumulation rate of 0.2674 mm/a. A thermal anomaly under Chasma Borealis is not considered, so that the geothermal heat flux is equal to 35 mW/m² everywhere.

The result of the reference simulation is an almost axi-symmetric ice cap centered at the north pole with an area of 0.998×10^6 km² and a volume of 1.6647×10^6 km³. Thus, the overall shape of the ice cap is modelled well, whereas medium- and small-scale structures like Chasma Borealis and the spiralling pattern of surface troughs are not reproduced. The maximum basal temperature (relative to the pressure melting point) is $T_{b,max} = -69.30^\circ\text{C}$, and the maximum surface velocity is $v_{s,max} = 0.66$ mm/a (very slow glacial flow, four to five orders of magnitude slower than typical values for terrestrial ice sheets).

Simulations with thermal anomaly. In addition to the set-up of the reference simulation, a thermal anomaly (increased heat flux, q_{CB}) is now considered under the entire area of Chasma Borealis.

Thermal anomaly always active. Runs #1–5 have been carried out with $q_{CB} = 100, 150, 200, 500$ mW/m² and 1 W/m², respectively, active throughout the simulation time of 5 Ma. For run #1, the basal temperature does not reach the melting point ($T_{b,max} = -33.56^\circ\text{C}$),

and the surface velocity in the chasm region increases only slightly ($v_{s,max} = 1.91$ mm/a). For runs #2–5, the basal temperature in the chasm region is at the melting point, and $v_{s,max}$ reaches values of the order of 10 mm/a. Runs #2 and 3 only produce a small topographic depression, whereas runs #4 and 5 produce a depression similar to the real chasm. For the result of run #5 see Fig. 1.

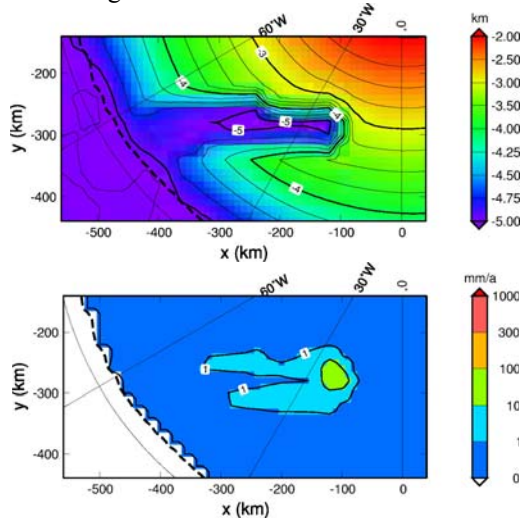


Fig. 1: Surface topography (top) and velocity (bottom) for run #5 ($q_{CB} = 1$ W/m²) and $t = 0$ (present).

Thermal anomaly temporarily active. It is now assumed that the thermal anomaly was only active during a limited period in the past. For run #6, $q_{CB} = 1$ W/m², active during the last 500 ka, and for run #7, $q_{CB} = 10$ W/m², active during the last 100 ka. For the present, both runs produce a fully developed chasm similar to the one shown in Fig. 1 and a maximum surface velocity $v_{s,max}$ of approximately 30 mm/a. Figure 2 shows the maximum basal temperature and water discharge rate for run #7. The by ≈ 30 ka delayed reaction of the basal temperature is due to imposing the heat flux 5 km below the ice base (which is debatable). The melting point is reached at $t = -54$ ka, and from then on the chasm forms. The basal melting rate (meltwater drainage) peaks at $t = -27$ ka at a value of 0.635 km³/a, which is a considerable amount, but still far away from constituting a catastrophic outflow event.

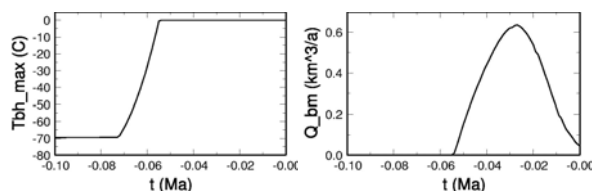


Fig. 2: Maximum basal temperature (left) and water discharge rate (right) for run #7 between $t = -100$ ka and $t = 0$.

Further, the maximum surface velocity reaches its largest value of 529 mm/a at $t = -53$ ka, shortly after the first occurrence of basal-melting conditions.

Chasm closure. Run #8 focuses on the closure of the chasm after the shutdown of the thermal anomaly. Like for run #7, $q_{CB} = 10$ W/m², but the active period is now between $t = -1$ Ma and -0.9 Ma. Figure 3 shows the maximum basal temperature and surface velocity. Evidently, the basal temperature drops to very low values within some 100 ka after the shutdown of the anomaly (the oscillations are due to the 125-ka obliquity cycle), and the accelerated ice flow stops almost immediately. Therefore, until $t = 0$ no significant closure of the chasm takes place.

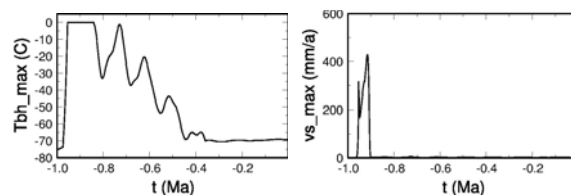


Fig. 3: Maximum basal temperature (left) and maximum surface velocity (right) for run #8 between $t = -1$ Ma and 0.

Conclusions. (i) A thermal anomaly with a heat flux of ≥ 500 mW/m² leads to the formation of a topographic depression similar to Chasma Borealis.

(ii) Simulated discharge rates are of the order of 1 km³/a. Catastrophic outflow would require either more extreme events or subglacial storage of water (jökulhlaup).

(iii) If the thermal anomaly is switched off, the chasm closes at an extremely slow rate.

References. [1] Fishbaugh K. E. and Head J. W. (2002) *JGR* 107, 5013. [2] Greve R., Mahajan R. A., Segsneider J. and Grieger B. (2004) *Planet. Space Sci.* 52, 775-787. [3] Greve R. (2006a) *ILTS Research Fund, Report, May 2006*, pp. 43-47. Institute of Low Temperature Science (ILTS), Hokkaido University, Sapporo, Japan. [4] Laskar J. and 5 others (2004) *Icarus* 170, 343-364. [5] Grieger B. (2004) pers. comm. [6] Greve R. and Mahajan R. A. (2005) *Icarus* 174, 475-485. [7] Le Meur E. and Huybrechts P. (1996) *Ann. Glaciol.* 23, 309-317. [8] Greve R. (2001) *Continuum Mechanics and Applications in Geophysics and the Environment*, Springer, pp. 307-325. [9] Greve R. (2006b) *GAMM-Mitteilungen* 29, 29-51. [10] Zuber M. T. and 20 others (1998) *Science* 282, 2053-2060. [11] Smith D. E. and 18 others (1999) *Science* 284, 1495-1503.

Additional Information. A PDF version of this paper with colour figures is available online at R.G.'s website (<http://www.ice.lowtem.hokudai.ac.jp/~greve/>) under the item "Publications".

PHOTOMETRIC SIGNATURES OF LIQUID WATER IN JSC MARS-1 REGOLITH SIMULANT. K. Gunderson¹, B. Lüthi¹, P. Russell¹ and N. Thomas¹. ¹Physikalisches Institut, University of Bern, Sidlerstrasse 5, CH-3012 Bern, Switzerland (kurt.gunderson@luethi@patrick.russell@nicolas.thomas@space.unibe.ch).

Introduction: Subsurface polar ice deposits are believed to exist on Mars. Their existence has been predicted [1] and also has been inferred from remote sensing instruments [2–4]. Because of the low mean surface temperatures and low mean atmospheric pressures, liquid water might not be expected to exist on Mars. However, models suggest that solar heating can raise temperature and pressure conditions across much of the Martian surface such that the triple point of water can be exceeded without reaching the boiling point, especially if the water contains dissolved salts [5]. Laboratory simulations support this prediction [6]. Near the poles the solar heating conditions that could lead ice to melt are less likely to occur than in equatorial regions but, under consideration of evidence for recent volcanic activity on Mars [7–8], it is conceivable that geothermal sources could melt ice in localized polar regions and lead to short lived surface seepage.

As demonstrated in Figure 1, liquid water has a tendency to darken soils that absorb it. We attempt to quantify this darkening effect by comparing the bidirectional reflectance distribution functions (BRDFs) of dry and wet JSC Mars-1 regolith simulant [9] in a variety of optical bandpasses. The associated reflectance signatures of moisture in a regolith simulant could help identify regions of surface moisture, if they exist, in visible or near infrared (NIR) images of Mars.



Figure 1. Wet (*left*) and dry (*right*) JSC Mars-1 simulant.

Data and analysis: Measurements were made using the Physikalisches Institut Radiometric Experiment (PHIRE) [10]. PHIRE is a goniometer experiment that can illuminate and observe a test sample over a broad range of measurement geometries. The measurements described here were performed at an incidence angle of $i=50$ deg and over a range of in-plane phase angles from $2 \leq g \leq 130$ deg. Eight broadband optical filters, covering blue to NIR wavelengths, provided wavelength control over the illuminating beam. The filter set included both astronomical standards and analogs to the filter set being used by the HiRISE experiment

[11] aboard the Mars Reconnaissance Orbiter, and is summarized in Table 1. Hapke reflectance models [12] were fit to the data using six free parameters. Reduced BRDF data are shown in Figures 2 and 3 with model fits overplotted. Discrepancies between the models and data are typically less than a part in 100. The most striking difference between the BRDFs of the dry and

Table 1. Summary of the optical filter set.

Effective wavelength	Description
462 nm	Johnson <i>B</i> .
503 nm	HiRISE blue-green analog (B_{HR}).
558 nm	Johnson <i>V</i> .
672 nm	Johnson <i>R</i> .
736 nm	HiRISE red analog (R_{HR}).
777 nm	Kron-Cousins red (R_{KC}).
875 nm	Johnson <i>I</i> .
926 nm	HiRISE NIR analog (I_{HR}).

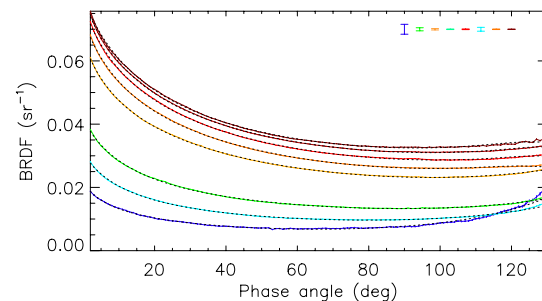


Figure 2. Measured BRDFs of dry JSC Mars-1 regolith simulant (*colored lines*) with reflectance models overplotted (*dotted*). Colors and effective wavelength values (nm) are: Blue=462, light blue=503, green=558, yellow-orange=672, orange=736, red=777, brown=875, dark brown=926. Systematic error bars are in the upper right hand corner.

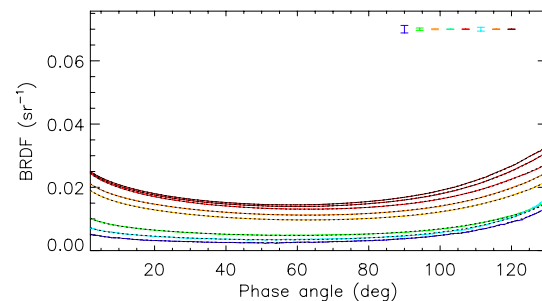


Figure 3. Same as Figure 2, but for wet JSC Mars-1 simulant.

wet samples is the relative weakness of the opposition surge in the wet sample. This is unusual for planetary regoliths and laboratory simulants.

Discussion: Figures 4 and 5 show a comparison of the JSC Mars-1 albedo measurements of [9] with albedo extrapolations of our best-fitting reflectance models to zero phase angles. The agreement between the measurements of [9] and our measurements of the dry simulant supports the validity of the PHIRE data. Discrepancies are most likely attributable to systematic uncertainties in the illumination source's output spectrum and photodiode QE, both of which were taken from vendor documentation to determine the effective wavelength values in Table 1. Also shown is a comparison between the regolith simulant measurements and measurements of dark and bright regions of the actual Martian surface [13]. The simulant is consistently darker than both the dry sample and a typical dark Martian surface region in all optical bandpasses.

Figure 6 shows the ratio of the BRDF of dry simulant to wet simulant. These data suggest that, if viewed from an orbiting platform, the brightness contrast between a localized region of wet regolith surrounded by mineralogically similar dry regolith would be stronger at low phase angles. At high phase angles, however, the wet and dry regions would be nearly equally bright. Contrast also appears higher at shorter wavelengths, but the significance of this wavelength trend is less certain because of systematic uncertainties in the data reduction methodology.

Conclusions: Photometric measurements of dry and wet Martian regolith simulant have been used to explore how localized regions of surface moisture on Mars might appear in visible/NIR images. The data, as expected, show that a wet region in a mineralogically uniform regolith would appear darker than the surrounding dry material. However, the brightness contrast would be expected to be strongest at shallow phase angles and absent at phase angles around 130 deg. Additionally, contrast might be stronger at short visible wavelengths than at NIR wavelengths. Although a detection of these signatures would not prove the presence of liquid water, they might be useful for constraining interpretations of surface contrast that, if found, are suggestive of liquid water's presence.

References: [1] Mellon M. T. and Jakosky B. M. (1995) *JGR*, 100, 11781–11799. [2] Feldman W. C. et al. (2002) *Science*, 297, 75–78. [3] Mitrofanov et al. (2002) *Science*, 297, 78–81. [4] Boynton et al. (2002) *Science*, 297, 81–85. [5] Haberle R. M. et al. (2001) *JGR*, 106, 23317–23326. [6] Sears D. W. G. and Chittenden J. D. (2005) *GRL*, 32, 23203. [7] Garvin J. B. et al. (2000) *Icarus*, 145, 648–652. [8] Márquez A. et al. (2004) *Icarus*, 172, 573–581. [9] Allen C. C. et al.

(1997) *LPS XXVIII*, Abstract#1797. [10] Gunderson K. et al. (2006) *Planet. Space Sci.*, in press. [11] McEwen A. S. et al. (2006) *JGR*, in press. [12] Hapke B. (1993) *Theory of reflectance and emittance spectroscopy*. University Press: Cambridge. [13] Mustard J. F. and Bell J. F. (1994) *GRL*, 21, 353–356.

Acknowledgements: This work has been funded through a grant from the Swiss National Fond.

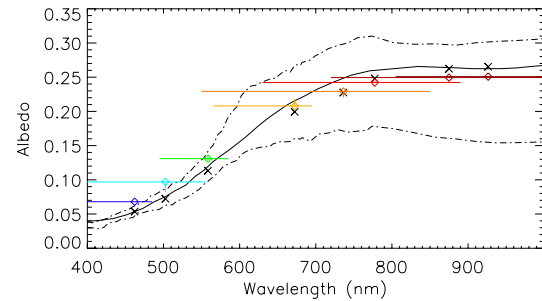


Figure 4. Dry simulant albedo measurements (diamonds) with filter FWHM bandpasses overplotted as horizontal bars and systematic errors as vertical bars. Colors are the same as Figures 1 and 2. *Solid:* simulant spectrum according to [9]. *X's:* Spectrum of [9] run through the PHIRE instrument response model. *Dot-dash:* Typical spectra of bright and dark Martian terrains [13].

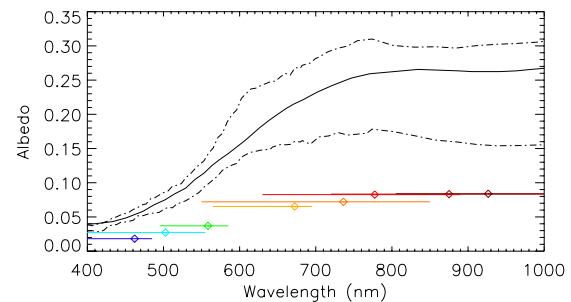


Figure 5. Same as Figure 4, but for the wet simulant.

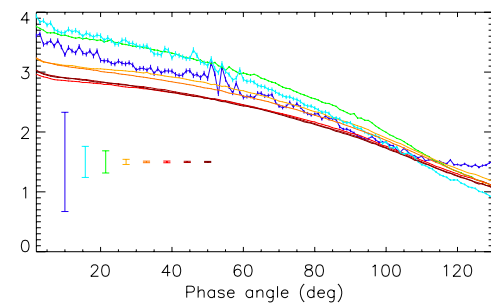


Figure 6. Dry:wet BRDF ratios. Statistical errors are overplotted as horizontal lines, and systematic errors are shown as error bars in the lower left.